

JET FRAGMENTATION AND PREDICTIONS OF THE RESUMMED
PERTURBATIVE QCD

By

ALEXEI N. SAFONOV

A DISSERTATION PRESENTED TO THE GRADUATE SCHOOL
OF THE UNIVERSITY OF FLORIDA IN PARTIAL FULFILLMENT
OF THE REQUIREMENTS FOR THE DEGREE OF
DOCTOR OF PHILOSOPHY

UNIVERSITY OF FLORIDA

2001

To my parents, Ludmila Dmitriyevna and Nikolay Sergeyevich Safonov.

ACKNOWLEDGMENTS

Most of all, I am very grateful to Prof. Andrey Korytov, the chair of the dissertation committee, for his invaluable contribution to the successful completion of this dissertation. Dr. Korytov's desire to share his experience and genuine dedication to physics were the key factors that defined the outcome of this work.

I am very thankful to Prof. Guenakh Mitselmakher for his advice, help and many hours of very useful discussions.

I would like to thank Dr. Joey Huston (Michigan State University), Dr. Valery Khoze (Durham University, UK), Dr. Steve Kuhlmann (Argon National Accelerator Laboratory), Dr. Avi Yagil (Fermi National Accelerator Laboratory) for their help and useful suggestions that were very important at different stages of this work

I appreciate the opportunity I had to work and collaborate with Dr. Serguei Klimenko (University of Florida), Dr. Jaco Konigsberg (University of Florida), Dr. Andrei Nomerotski (Fermilab) and many other people working at the CDF Experiment, who contributed into the successful completion of this dissertation.

I am thankful to Ben Kilminster (University of Rochester) and Slava Krutelyov (Texas A&M University) for carefully reading the manuscript and their helpful suggestions.

During my study at the University of Florida, I very much enjoyed the lectures of Zongan Qiu, Charles Hooper and Charles Thorn, and I believe that those were a large factor in the successful completion of this work.

TABLE OF CONTENTS

	<u>page</u>
ACKNOWLEDGMENTS	iii
ABSTRACT	vii
CHAPTERS	
1 QUANTUM CHROMODYNAMICS AND JET FRAGMENTATION	1
1.1 Perturbative QCD	2
1.2 Resummed QCD Calculations and Applicability for Jet Fragmentation	4
1.2.1 Modified Leading Log Approximation (MLLA)	6
1.2.2 Local Parton-Hadron Duality Hypothesis (LPHD)	9
1.3 MLLA Predictions	10
1.3.1 Momentum Distribution of Partons in Jets	10
1.3.2 Mean Charged Particle Multiplicity	11
1.3.3 On Differences Between Quark and Gluon Jets	12
1.3.4 Next-to-MLLA Corrections	13
2 EARLY EXPERIMENTAL RESULTS AND MOTIVATION	15
3 CDF AT FERMILAB: EXPERIMENTAL FACILITY OVERVIEW	17
3.1 Collider Detectors in High Energy Physics	18
3.2 Collider Detector at Fermilab: Design and Overview	19
3.2.1 Vertex Detectors (VTPC and SVX)	20
3.2.2 Central Tracking Chamber (CTC)	21
3.2.3 Electromagnetic and Hadronic Calorimeters	22
3.2.4 Other Sub-Detectors	23
3.3 CDF Data Readout and Processing	24
4 DATA ANALYSIS TOOLS	26
4.1 Monte-Carlo Event Generators	26
4.2 Detector Simulation	28
5 FEASIBILITY OF THE JET FRAGMENTATION STUDIES AT CDF	30

6 DATA SELECTION, CORRECTIONS AND ERROR ESTIMATES	33
6.1 Data Selection and Quality Cuts	33
6.2 Corrections to the Data	36
6.2.1 Jet Corrections	36
6.2.2 Tracking Corrections	39
6.3 Systematic Uncertainties and Methods of Evaluation	42
6.3.1 Systematics Associated with the Calorimetry	43
6.3.2 Systematics Associated with the Tracking	47
7 RESULTS AND COMPARISONS TO THE PREDICTIONS OF THE MODIFIED LEADING LOG APPROXIMATION (MLLA).	48
7.1 Measurement of the Momentum Distribution of Charged Particles in Jets	49
7.1.1 Fits of the Distributions with the MLLA Limiting Spectrum	49
7.1.2 Q_{eff} from the MLLA Fit	54
7.1.3 Fit for the Peak Position of the Distributions. MLLA Scaling. Extraction of Q_{eff}	55
7.1.4 Dependence of the Fitted Parameter K on the Size of the Cone	57
7.1.5 Extraction of the LPHD Parameter $K_{LPHD}^{charged}$ and the Ratio of Multiplicities in Gluon and Quark Jets r	59
7.1.6 Summary	61
7.2 Measurement of the Inclusive Charged Particle Multiplicity. Comparisons to the MLLA Predictions. Extraction of the Ratio r and LPHD Parameter $K_{LPHD}^{charged}$	62
7.3 Comparison of the Photon+Jet and the Dijet Data. Model-independent Measurement of the Ratio of Multiplicities in Gluon and Quark Jets r	66
7.4 Particle Properties in Jets and Comparisons to Herwig Monte-Carlo	69
7.4.1 Mean Charged Multiplicity	70
7.4.2 $dN/d(k_T)$ Distribution	72
7.4.3 $dN/d(\log p)$ Momentum Distribution	74
7.4.4 Multiplicity Flow $dN/d\theta$	76
7.5 Conclusions	77
8 SUMMARY OF THE EXPERIMENTAL RESULTS AND THEIR IMPACT ON UNDERSTANDING OF JET FRAGMENTATION. FUTURE PERSPECTIVES	79
APPENDIX ANALYSIS OF THE CENTRAL TRACKING CHAMBER (CTC) RECONSTRUCTION EFFICIENCIES	83
Track Embedding Method and Monte-Carlo Testing	84
Track-Finding Algorithm	88
Results and Cross-Checks	93
Conclusion And Limits of Applicability	98

LIST OF REFERENCES	100
BIOGRAPHICAL SKETCH	105

Abstract of Dissertation Presented to the Graduate School
of the University of Florida in Partial Fulfillment of the
Requirements for the Degree of Doctor of Philosophy

JET FRAGMENTATION AND PREDICTIONS OF THE RESUMMED
PERTURBATIVE QCD

By

Alexei N. Safonov

May 2001

Chairman: Andrey Korytov

Major Department: Department of Physics

This dissertation is dedicated to the experimental analysis of jet fragmentation, the process of formation of jets of particles produced in high-energy collisions, and to the comparison of the results to the predictions of resummed perturbative calculations within Quantum Chromodynamics. Data used in this analysis were obtained by the Collider Detector at Fermilab (CDF) Experiment in proton-antiproton collisions with the center-of-mass energy 1.8 TeV produced by the Tevatron collider at Fermi National Accelerator Laboratory.

Jet fragmentation, because of its softness (typical transverse momenta of particles in jets with respect to the jet axis is 200-300 MeV), was long considered as an essentially non-perturbative, and thus incalculable, QCD process. Recent calculations performed in the framework of Modified Leading Log Approximation (MLLA) have made an attempt

to expand the perturbative domain to include the fragmentation phenomenon. Validity of the MLLA approach can only be verified experimentally.

Early experimental measurements have shown a good qualitative agreement between the lower energy data and the MLLA predictions. However, some of these results appeared to contradict each other.

Studies presented in this work significantly expand the area of the fragmentation studies by analyzing a much wider range of jet energies, reaching far beyond what could be achieved at e^+e^- colliders. They also provide a good testing ground for the universality of the jet properties at e^+e^- and hadron collisions. Important MLLA predictions of scaling were studied for the first time and found to be supported by the data.

The analysis presented in this work shows a high level of consistency between the data and the MLLA predictions. This proves that the jet fragmentation is largely a perturbative process in agreement with the assumptions that are the basis of MLLA. Essential model parameters are extracted and extensive cross checks of the model self-consistency were performed.

CHAPTER 1

QUANTUM CHROMODYNAMICS AND JET FRAGMENTATION

For the last 30 years, there has been an agreement that all the matter of the Universe is built of fermions (leptons and quarks) that interact with each other via the vector boson exchange. These interactions are described by gauge theories, and to properly describe a particular interaction, one needs to find an appropriate gauge symmetry and a particular representation of the theory.

All leptons are divided into three generations: the first generation consists of the electron and electron neutrino (e^- and ν_e), the second of the muon and muon neutrino (μ^- and ν_μ), and the third of the tau and tau neutrino (τ^- and ν_τ). The same is true for quarks: the first generation of quarks consists of u and d-quarks, the second of c- and s-quarks, and the third of t- and b-quarks.

Three known kinds of interactions, apart from gravitation, are electromagnetic, weak and strong interactions. Electromagnetic interaction involves electrically charged particles (all fermions except neutrinos) and the corresponding exchange boson is photon (γ). The weak interaction is responsible for the well-known radioactive beta decay processes and involves all fermions mentioned above; the weak interaction is mediated by three bosons: W^+ , W^- and Z . The strong interaction is the interaction between the nuclei constituents (quarks and gluons) and is responsible for keeping nuclei constituents together. The strong interaction involves all quarks and is mediated by gluons (there are 8 different species of gluons).

The electromagnetic and weak interactions are the oldest known interactions and are the best studied and understood. The Standard Model of Electroweak Interactions [1] defines the dynamics of both the participating particles and the exchange vector bosons. It allows the calculation of cross-sections of different processes with a high precision (sometimes it requires sophisticated calculations, but there is a well-defined systematic procedure of performing such calculations). The Standard Model is tested in various experimental studies and shows a very high level of consistency with the data, even though the last particle comprising the Standard Model, the Higgs boson responsible for generation of particle masses, has not yet been found. The experimental finding of the Higgs boson is one of the most important discoveries yet to be made by the high-energy physics, and a lot of effort and resources are applied in this direction.

The strong interaction is strikingly different from the electromagnetic and weak forces because its strength becomes larger and grows very quickly with the distance between the interacting quarks, while it almost disappears when the distance becomes small. This effect is called asymptotic freedom. Both electromagnetic and weak interactions show different behavior: their strength rapidly falls with distance.

1.1 Perturbative QCD

Early experiments of proton-proton scattering [2] showing a low rate at large scattering angles were interpreted to suggest that the proton consists of an ensemble of loosely bounded cloud of non-interacting constituents incapable of absorbing a large momentum transfer. However, later deep-inelastic scattering (scattering of an electron on a proton) studies [3] have shown a substantial rate of high momentum-transfer

interactions, inconsistent with this hypothesis and, therefore, have rejected the initial picture of the strong interactions. It also revealed the so-called Bjorken scaling [4]. Bjorken scaling essentially says that the proton structure, as seen by the electron, does not depend on the momentum transfer. Later, Bjorken [4] and Feynmann [5] proposed the model of asymptotically free partons. However, at that time no gauge symmetry was known to carry the feature of asymptotic freedom.

In parallel, Gell-Mann and Zweig, based on the studies of hadron spectroscopy, suggested a quark model with then three (u-, d-, s-, the other three quarks, c-, b-, and t, were discovered much later) species of quarks [6]. However, this model, to not contradict Fermi-Dirac statistics, required the introduction of a new, seemingly unnatural, quantum number – “color”, proposed by Han, Nambu and Gell-Mann [7].

In the early 1970s, Pollitzer, Gross and Wilczek discovered the existence of asymptotically free field theories [8] among the class of non-Abelian gauge theories. It appeared natural to assign the color to be the gauge quantum number, and the total symmetry to the local gauge group SU(3). The model became known as Quantum Chromodynamics (QCD).

The solution of the renormalization group equation leads to the following form of the running coupling constant α_s (to one loop) [8]:

$$\alpha_s = \frac{1}{b_0 \ln(Q/\Lambda)}$$

where $b_0 = 11 - 2/3 n_f$, n_f – number of quark flavors, Q is the momentum transfer, and Λ is a parameter having the dimension of energy that comes from the renormalization procedure and depends on the renormalization scheme.

Experimental measurements of the mass scale Λ (in the modified minimal subtraction scheme [9]) yield values of around 200 MeV [10]. The form of the coupling constant suggests that the perturbation theory is valid (α_s is small) only when Q is larger than about 1 GeV.

1.2 Resummed QCD Calculations and Applicability for Jet Fragmentation

When using perturbative QCD for parton-splitting problems, such as parton branching, one has to remember that “parton counting” depends on the resolution (the smaller the spatial scale of the probing, the more partons will be resolved). Technically, this means the importance of taking into account large logarithmic corrections of the form $\alpha_s \ln Q$.

At large Q , even though the running coupling is small, the logarithm can be large, making the product $\alpha_s \ln Q$ of the order of 1. Such logarithmic corrections appear in all orders and require resummation of their contributions. This means that the fixed-order calculations in perturbation theory are just not sufficient for reliable predictions. The physical sense of this is that QCD parton multiplication processes have large probabilities and this fact needs to be properly handled.

For the case of deep inelastic scattering, similar logarithmic corrections appear (scaling violation [11]) and reflect the fact that by increasing Q , one increases the resolution of the probing of the scattering quark or gluon, and starts seeing finer substructure of the virtual parton, observing more and more gluons sitting there, similar to the well-known example of equivalent photons in QED.

The Leading Log Approximation (LLA) [12] was developed to quantify the expected logarithmic violation of the Bjorken scaling. In the LLA, one keeps track of contributions to the structure function of the order

$$W(x, Q^2) = \sum_n f_n \frac{\alpha_s}{\pi} \ln^n(Q^2)$$

and neglects terms without large log.

The Double Logarithmic Approximation (DLA) [13] emerged when first attempts to understand the dynamics of soft particles in jets were made. DLA was used for pure gluonic system and was keeping track of contributions (for each splitting) of the order $\alpha_s \ln^2(Q^2)$ and neglecting contributions of the order $\alpha_s \ln(Q^2)$ and α_s .

It was found that color coherence effects result in a strong “angular ordering” [14] in QCD bremsstrahlung. Angular ordering means that the sum of the diagrams corresponding to consecutive emissions of gluons of a parent parton are equivalent (within the DLA precision) to one diagram with angular ordered emissions, as illustrated on Figure 1.1. This was a very important observation that allowed significant simplification of resumming large contributions into the scattering amplitude in all orders. Again, a similar effect of enhancement of particularly “ordered” emissions can be found in QED with the example of equivalent photons.

The DLA approach, even though it revealed many important features of the parton cascade development, was not very successful in providing quantitatively reasonable predictions. To properly correct the DLA, one had to include Single Log contributions. Because of the similarities of this new scheme to the standard Leading Log

Approximation, this improved approximation was called Modified Leading Log Approximation (MLLA) [15].

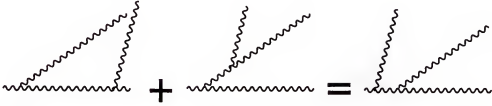


Figure 1.1: Angular Ordering results in effectively producing the consecutive emissions at smaller and smaller angles with respect to the parent parton.

1.2.1 Modified Leading Log Approximation (MLLA)

Inclusion of the Single Logarithmic effects results in a large increase of the number of interference diagrams that need to be analyzed.

The only MLLA parameter, Q_{eff} , serves to regularize the soft and collinear divergences, being a cut-off on the minimal allowed parton transverse momentum (with respect to the parent parton). At the same time, it sets a lower limit on the parton mass playing the role of an effective parton mass.

Q_{eff} can be viewed as the scale that separates perturbative parton showering from the stage of non-perturbative soft hadronization. In other words, a gluon emitted with $k_T \sim Q_{eff}$ can hardly be treated as a gluon at all, as it is immediately forced to hadronize. The value of Q_{eff} is not defined in the model and has to be found experimentally. A relatively low value of Q_{eff} is strongly preferred. If Q_{eff} is large, the number of partons, at currently achievable jet energies, is low and the transition of these “partons” into soft hadrons will be fully in hands of the phenomenological hadronization model. This can be

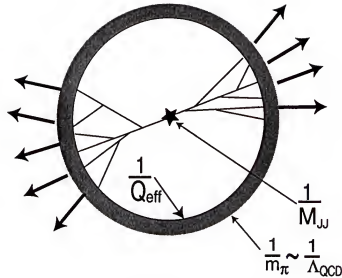


Figure 1.2: Depiction of the jet fragmentation. There are three scales in the problem: the hard-scattering scale M_{JJ} , scale Q_{eff} at which perturbative parton branching stops and the hadronization starts, and, finally, the scale at which the formation of hadrons is finished and that has the order of light hadron mass m_π . The lower the Q_{eff} , the smaller the region of phenomenological hadronization, and larger the role of the perturbative stage.

pictured as it is shown on Figure 1.2: if Q_{eff} is high, the area of our ignorance (phenomenological hadronization region between perturbative partons and final hadrons) is wide and may dominate over the perturbative effects making these calculations completely useless. However, if the Q_{eff} is low (200-400 MeV), this area shrinks and the influence of the perturbative stage will grow. Together with the Local Parton-Hadron Duality hypothesis, discussed in the next section, that assumes local hadronization, MLLA has a chance to end up being a model that can coherently describe the jet fragmentation.

Figure 1.3 shows the distribution of the transverse, with respect to the jet direction, momentum of the particles in jets. Note that with the conventional cut-off of the order of 1 GeV, the vast majority of particles are not accounted for by the

perturbative description. To be successful, any model of the jet fragmentation inevitably has to be able to deal with sufficiently low (of the order of a few hundred MeV) momentum transfers.

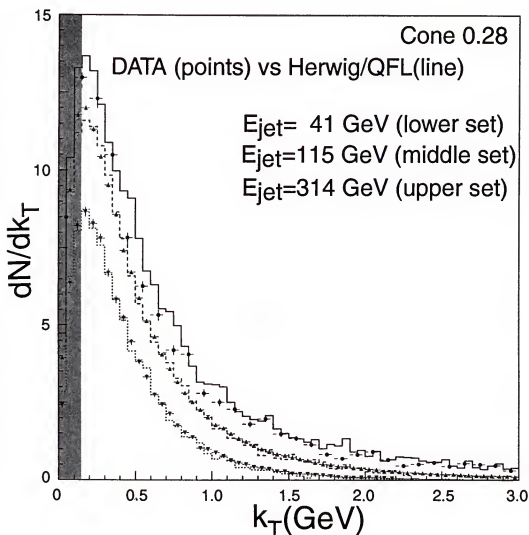


Figure 1.3: The distribution of the transverse (with respect to the jet direction) momenta of particles in jets for dijet events. Only charged particles within a cone of size 0.28 rad around the jet are counted. Three different dijet masses are compared to the predictions of Herwig 5.6 Monte-Carlo. The shaded area corresponds to the region where track parameters cannot be measured correctly due to looping of the track in the magnetic field.

1.2.2 Local Parton-Hadron Duality Hypothesis (LPHD)

LPHD hypothesis [16] assumes that the hadronization, the process of formation of colorless hadrons from the QCD partons, is local and happens at the end of the parton showering.

The key assumption of the LPHD is that the conversion of partons into hadrons occurs at a low virtuality scale, of the order of hadronic masses, independent of the primary hard process, and involves only low momentum transfers [17]. Such local duality is naturally connected with the “pre-confinement” properties [18] of the QCD cascades, which ensures that the colors are locally compensated.

This effectively means that the properties of hadrons are closely related to the partons they originate from and that the collective effects of color exchanges with partons producing other hadrons are small. It is true that parton distributions are smeared by low k_T exchanges and, on an event-by-event basis, hadron distributions differ from the parton ones. However, according to LPHD, sufficiently inclusive distributions that are averaged over many events should reproduce the original parton distributions.

In its simplest interpretation, LPHD predicts that the momentum distributions of hadrons and partons in jets are identical apart from a possible normalization. The same will be true for inclusive mean particle multiplicity and can be written as:

$$N_{gluon}^{hadrons} = K_{LPHD} N_{gluon}^{partons}$$

LPHD is asymptotically correct: i.e., it becomes exact in the limit of infinite jet energies. Therefore, it should work well enough at sufficiently high jet energies. Quantification of the term “sufficiently high” can only be made experimentally.

1.3 MLLA Predictions

In this section, particular predictions of the Modified Leading Log Approximation that can be verified experimentally and are relevant to this work are discussed. Most of the MLLA predictions are presented for a gluon jet, and the third sub-section discusses how these can be reapplied to the quark jet.

1.3.1 Momentum Distribution of Partons in Jets

MLLA+LPHD scheme gives a very firm and experimentally verifiable prediction for the shape of the inclusive momentum distribution of particles in jets. The momentum distribution of partons in a gluon jet within a restricted cone of size θ_c around the jet axis is given by [15]:

$$\frac{dN_{\text{partons}}^{\text{gluon}}}{d\xi} = \frac{4N_c}{b} \Gamma(B) \left[\frac{\pi/2}{-\pi/2} \frac{d\tau}{\pi} \left[\frac{\cosh \alpha + (1 - 2\zeta) \sinh \alpha}{\frac{4N_c}{b} Y \frac{\alpha}{\sinh \alpha}} \right]^{B/2} \right] \times \quad (1.1)$$

$$\times e^{-B\alpha} I_B \left(\sqrt{\frac{4N_c}{b} Y \frac{\alpha}{\sinh \alpha} (\cosh \alpha + (1 - 2\zeta) \sinh \alpha)} \right),$$

with important variables:

$$\xi = \ln \frac{1}{x}, \quad x = \frac{p}{E_{\text{jet}}}, \quad Y = \ln \frac{E_{\text{jet}} \theta_{\text{cone}}}{Q_{\text{eff}}},$$

where B and b are QCD constants ($B=101/81$ and $b=9$ for the number of colors $N_c=3$ and the number of effectively massless quarks $N_f=3$), and I_B is the modified Bessel function of order B .

Other variables are defined as follows:

$$\zeta = 1 - \frac{\xi}{Y}, \quad \alpha = \alpha_o + i\tau, \quad \tanh \alpha_o = 2\zeta - 1$$

MLLA calculations are carried out in the assumption $x \ll 1$. Transition to the particle-level distribution utilizes the LPHD hypothesis and can be expressed as:

$$\frac{dN_{gluon}^{hadrons}}{d\xi} = K_{LPHD} \frac{dN_{gluon}^{partons}}{d\xi}, \quad (1.2)$$

The peak position of the momentum spectrum is given in MLLA by [19]:

$$\xi_o = \frac{1}{2}Y + \sqrt{cY} - c, \quad \text{where } c = 0.29 \text{ for } n_f = 3 \quad (1.3)$$

The third term, the constant, just falls out of the MLLA spectrum function (1.1). Though, strictly speaking, the next-to-MLLA terms may contribute to the peak position at this level [19].

1.3.2 Mean Charged Particle Multiplicity

Mean parton multiplicity is nothing but an integration of the previous equation over ξ and can be expressed as the following [19]:

$$N_{gluon}^{partons} = \Gamma(B) \left(\frac{z}{2} \right)^{-B+1} I_{B+1}(z), \quad \text{where } z = \sqrt{16N_c Y/b} \quad (1.4)$$

The corresponding expectation for hadron multiplicity in a gluon jet is a trivial generalization of (1.2):

$$N_{gluon}^{hadrons} = K_{LPHD} N_{gluon}^{partons} \quad (1.5)$$

1.3.3 On Differences Between Quark and Gluon Jets

In MLLA, momentum distributions in quark and gluon jets are different only by a simple normalization factor r , equal to the ratio of gluon and quark color charges C_A/C_F [19]:

$$\frac{dN_{gluon}^{parton}}{d\xi} = \frac{dN_{quark}^{parton}}{d\xi} \times r \quad (1.6)$$

Then, for the ratio of multiplicities in gluon and quark jets, one will have:

$$N_{gluon}^{parton} = N_{quark}^{parton} \times r \quad (1.7)$$

For the case of jets that are a mixture of quark and gluon jets (like at the Tevatron), the prediction for the parton-level momentum distributions will take the form:

$$\frac{dN_{mix}^{parton}}{d\xi} = \epsilon_{gluon} \frac{dN_{gluon}^{parton}}{d\xi} + \epsilon_{quark} \frac{dN_{quark}^{parton}}{d\xi} \quad (1.8)$$

Using Eq. (1.6) and $\epsilon_{quark} + \epsilon_{gluon} = 1$, one obtains:

$$\frac{dN_{mix}^{parton}}{d\xi} = \epsilon_{gluon} \frac{dN_{gluon}^{parton}}{d\xi} + (1 - \epsilon_{gluon}) \frac{1}{r} \times \frac{dN_{quark}^{parton}}{d\xi} = \left(\frac{1}{r} + (1 - \frac{1}{r}) \epsilon_{gluon} \right) \frac{dN_{gluon}^{parton}}{d\xi} \quad (1.9)$$

Finally, to make this formula usable for real particles, one needs to apply the LPHD hypothesis Eq. (1.5):

$$\frac{dN_{mix}}{d\xi} = K_{LPHD} \times \left(\frac{1}{r} + (1 - \frac{1}{r}) \epsilon_{gluon} \right) \frac{dN_{gluon}^{parton}}{d\xi} \quad (1.10)$$

The result for the multiplicity is a trivial integration of Eq. (1.10):

$$N_{mix} = K_{LPHD} \times \left(\frac{1}{r} + (1 - \frac{1}{r}) \epsilon_{gluon} \right) N_{gluon}^{parton} \quad (1.11)$$

1.3.4 Next-to-MLLA Corrections

Strictly speaking, the next-to-MLLA calculations are not the next order calculation of the contributions into the amplitudes of the branching processes. Instead, the term “next-to-MLLA” conventionally refers to “improved” solutions of the same primary MLLA evolution equations.

The effect of the next-to-MLLA corrections is an increase in the total multiplicity of partons in gluon and quark jets. These corrections can be represented by two modifications: parton multiplicity in a gluon jet must be scaled by the next-to-MLLA correction factor F_{nMLLA} , and the ratio of multiplicities in gluon and quark jets r deviates from its classical value of 9/4. Both F_{nMLLA} and r are weak function of the jet energy. The shape of the spectrum changes too, but this change is much less significant. Inclusion of these corrections modifies the formula for the momentum distribution as follows:

$$\left. \frac{dN_{mix}^{hadrons}}{d\xi} \right|_{next-to-MLLA} = F_{nMLLA} \times K_{LPHD} \times \left(\frac{1}{r} + \left(1 - \frac{1}{r}\right) e_{gluon} \right) \left. \frac{dN_{gluon}^{partons}}{d\xi} \right|_{MLLA} \quad (1.12)$$

Analogous relation is preserved for the multiplicity:

$$N_{mix}^{hadrons} \Big|_{next-to-MLLA} = F_{nMLLA} \times K_{LPHD} \times \left(\frac{1}{r} + \left(1 - \frac{1}{r}\right) e_{gluon} \right) N_{gluon}^{partons} \Big|_{MLLA} \quad (1.13)$$

It is convenient to rewrite the formulas as follows:

$$\left. \frac{dN_{mix}^{hadrons}}{d\xi} \right|_{next-to-MLLA} = K \times \left. \frac{dN_{gluon}^{partons}}{d\xi} \right|_{MLLA} \quad (1.14)$$

where

$$K = F_{nMLLA} \times K_{LPHD} \times \left(\frac{1}{r} + \left(1 - \frac{1}{r}\right) \epsilon_{gluon} \right) \quad (1.15)$$

There are several published calculations [20,21,22] of the correction factor F_{nMLLA} and the value of the ratio of multiplicities in gluon and quark jets, r . These papers use different methods of calculating the corrections, and there is a disagreement among them as to the exact values of F_{nMLLA} and r . However, they all agree that both parameters are practically constant for a wide range of energies, which allows them to be treated as constants. According to the three different calculations, the factor F_{nMLLA} takes values of 1.13 ± 0.02 [20], 1.50 ± 0.08 [21], and 1.40 ± 0.01 [22]. Ratio r , meanwhile, takes the values 1.75 ± 0.01 , 1.60 ± 0.05 and 1.79 ± 0.07 , respectively. The uncertainties shown with the values correspond to the range of changes in these parameters over the range of jet energies relevant to this study (roughly 40 to 300 GeV).

In this analysis, when extracting quantities from the experimental data that require knowledge of the correction factor F_{nMLLA} , the “average” value of $F_{nMLLA} = 1.3$ was used with a “theoretical uncertainty” of 0.2 to account for the apparent disagreement [20,21,22]. The ratio r was treated as a free parameter and its value was extracted from the data.

CHAPTER 2

EARLY EXPERIMENTAL RESULTS AND MOTIVATION

A number of publications [23, 24] coming from e^+e^- and ep experiments testing whether perturbative QCD can indeed handle jet fragmentation have appeared over the last ten years. Generally, they have shown that MLLA is rather successful in describing the hadron distributions in jets, and obtained a number of important results. However, some of the results appeared to be inconsistent and revealed some unanswered questions regarding the experimental procedure. This clearly calls for an independent verification of the MLLA predictions and a more thorough check of the consistency of the model with the experimental data.

A variety of predictions, such as $E_{jet}\theta_c/Q_{eff}$ (θ_c is the opening angle in which the hadrons are counted) scaling of the MLLA, have never been verified experimentally, nor was the consistency of the energy evolution of the results thoroughly checked.

In e^+e^- experiments, with their fixed center-of-mass energy, the range of available jet energies is very limited, as the majority of the data is represented by two-jet events with the energy of each jet being simply a half of the total energy. Use of the "Mercedes-like" three-jet events always results in a very limited dynamic range, given the relatively low center-of-mass energy. Several LEP experiments attempted to use these three-jet events to compare gluon and quark jets (at e^+e^- , the three-jet events are combinations of two quark and one gluon jet). However, the methods used for selecting

and separating the gluon jet are not straightforward. Results on the ratio of hadron multiplicities in gluon and quark jets, for the same ranges of energies, evolved very significantly from earlier measurements of $r \sim 1.0$ to the most recent of $r \sim 1.5$ with typically very small errors, indicating potential problems with the experimental procedure.

MLLA predictions regarding the evolution of the momentum distribution within restricted cones around jets were never experimentally verified at all. This would make an important measurement, given the role of angular variables in MLLA.

For years, it was a common belief that analyses of properties of particles in jets, such as the jet fragmentation studies, are best done at the e^+e^- machines with its clean environment and low backgrounds. However, apart from the obvious need for clarification of existing inconsistencies, there are clear advantages of performing such studies at hadron collider experiments. The much higher energies of the jets available at the Tevatron open a direct way for verifying the consistency of MLLA over a large range of jet energies, particularly with regard to the $E_{jet}\theta_c/Q_{eff}$ scaling suggested by MLLA. Quark and gluon jets are readily available in hadron collisions and allow the direct comparison of their properties without running into the necessity to use complicated techniques.

At CDF, previous jet fragmentation studies [25] were concentrated on verification of the approximate scaling behavior at the higher momentum region of the momentum spectrum and not in the region of the soft fragmentation. Early CDF studies of the jet shapes [26] had a limited coverage in terms of the jet energies and were only studying the transverse flow of the jet energy.

CHAPTER 3

CDF AT FERMILAB: EXPERIMENTAL FACILITY OVERVIEW

Collider Detector Facility at Fermilab (CDF) is one of the two major collider experiments (the other one is D0), located at the Fermi National Accelerator Laboratory (Batavia, IL). It detects events from the collision of proton and anti-proton beams produced by the Tevatron, the world's most powerful accelerator of colliding beams, with center-of-mass energy of 1.8 TeV and peak luminosity $L \sim 1.6 \cdot 10^{31} \text{ cm}^2\text{s}^{-1}$. In its nominal configuration, the Tevatron used 6 proton and 6 antiproton bunches with the beam revolution frequency 50 kHz.

CDF was built in the 1980's, detecting first proton-antiproton collisions in 1985. The first physics run with an essentially complete detector started in 1987. Since then, CDF underwent a number of upgrades designed to improve the capabilities of the detector by employing the latest technological advances to match the growing energy and luminosity of the beams produced by the Tevatron. Figure 4.1 shows the picture of the CDF detector (opened-up) in the assembly hall, giving a feel for the size and complexity of this five thousand ton high-precision device.

In 1994, CDF (simultaneously with D0) announced the discovery of the top-quark [27], the heaviest, and the last quark required to complete the family of quarks as prescribed by the Standard Model of elementary particles. Major advances were made in other areas of the experimental high energy physics, particularly in QCD, electroweak physics and exotic new particle searches.

3.1 Collider Detectors in High Energy Physics

In fixed-target experiments, the center-of-mass energy grows only as a square root of the original beam energy. With the technological obstacles of producing a beam of very high energy (large size, and cost, of the accelerator ring, complicated magnetic system etc.), any significant advance in the center-of mass energy would be very costly and all but impossible.

Colliders became a major step forward in experimental High Energy physics. Unlike the fixed-target case, the center-of-mass energy produced by colliding beams is twice the energy of the original beams and grows linearly with the energy. The introduction of colliders allowed a large increase in the center-of-mass energy, and, therefore, have paved the way for studying physics at much higher energy scale.

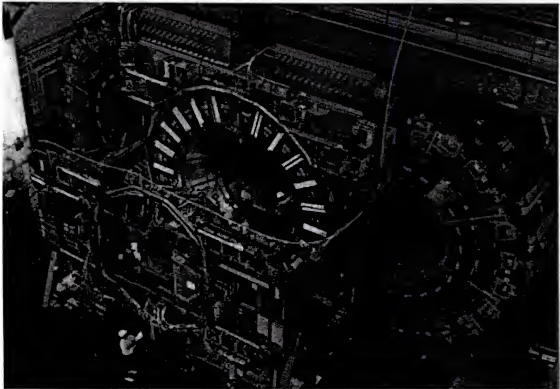


Figure 3.1: The view of the CDF Detector in the Assembly Hall during the maintenance.

3.2 Collider Detector at Fermilab: Design and Overview

CDF is a multipurpose collider detector serving for detection and identification of particles in high energy collisions. CDF has a number of major subsystems providing complementary measurements necessary to reconstruct the decay products of a proton-antiproton interaction. A detailed technical description of the CDF detector can be found elsewhere [28].

Figure 4.2 shows the drawing of one quarter of the CDF detector with the interaction point shown in the right lower corner. Major detectors that make up the CDF detector, starting from the interaction point, are:

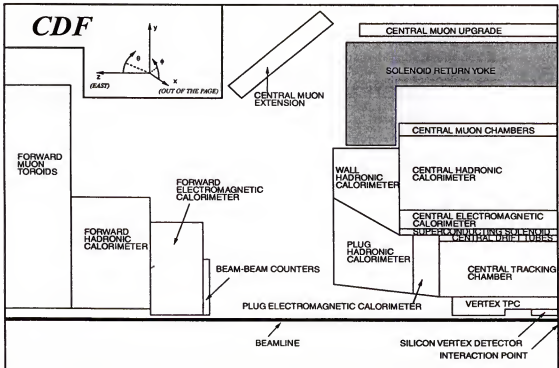


Figure 3.2. Drawing of the CDF detector. One quarter view.

- Silicon Vertex Detector (SVX) designed for precise measurement of the position of the interaction vertex in the r - ϕ plane.
- Vertex Tracking Detector (VTPC), a wire chamber, which measures the z -position of the interaction.
- Central Tracking Chamber (CTC), a multi-layer proportional chamber that measures the momentum and spatial parameters of the particle's trajectories (tracks) in the magnetic field ($B=1.4$ T).
- Full set of electromagnetic (EM) and hadronic (HA) calorimeters that measure the energy of the jets of particles produced in the collision.
- Muon System (made of layers of drift chambers and scintillators), positioned (partially) behind a special protective steel wall, which absorbs all particles that may escape the calorimeter except muons.

In the rest of this chapter a more detailed description, including the resolutions and essential parameters, of each of the CDF subsystems substantially used in this analysis is presented.

3.2.1 Vertex Detectors (VTPC and SVX)

The Silicon Vertex detector (SVX) is the closest component to the beam pipe. It is roughly 60 cm long and covers the radial region from 3.0 to 7.9 cm. It consists of several layers carrying silicon strips parallel to the beam line. The r - ϕ tracking allows a very precise measurement of the transverse position of the event vertex and contributes to the track momentum distribution (default tracking links Central Tracking track segments with the SVX hits). Surrounding the SVX is the Vertex Time-Projection Chamber

(VTPC). VTPC consists of an array of 8 adjacent (in z) drift chambers. VTPC provides r - z tracking information that is used to determine the position of the interaction in z -direction. Vertex information provided by SVX and VTPC is instrumental for a vast range of experimental studies.

3.2.2 Central Tracking Chamber (CTC)

The Central Tracker extends from a radius $r=31$ to $r=132$ cm, and is 3.2 m long barrel-shaped drift chamber. It has several layers of radial and stereo wires (stereo wires are tilted at 3 degree angle with respect to the radial wires). The amount of the material in front of the CTC (as seen from the interaction point) ranges from 4-6 radiation lengths in the central part (more than 30 degrees with respect to the beam line) and grows to about 10 radiation lengths for smaller angles at 20 degrees.

Table 3.1: Selected parameters of the CDF Central Tracking Chamber.

Number of layers	84
Number of superlayers	9 (5 axial + 4 stereo)
Drift field	~ 1350 V/cm
Resolution	< 200 μm per wire
Efficiency	> 0.98 per point
Double track resolution	< 5 mm or 100 ns
Maximum drift distance	40 mm
Maximum hits per wire	> 7
Z-resolution	4 mm
Momentum resolution	$\delta p_T / p_T \approx 0.002 \cdot p_T$
R_{max}	1.32 m
Magnetic field B	1.4 T

CTC is used to measure the momentum and spatial position of the particle trajectory by arranging hits produced by the passing particle into layer segments and then linking segments into a full trajectory. A Tracking algorithm then fits the obtained hits for the parameters of the track trajectory. This information allows precise reconstruction of the particle momentum and its spatial position inside the CDF detector. The momentum resolution of the CTC is better than $\delta p_T / p_T \approx 0.002 \cdot p_T$. Table 4.1 shows some of the essential parameters of the CTC.

3.2.3 Electromagnetic and Hadronic Calorimeters

The set of calorimeters consists of several electromagnetic and hadronic calorimeter systems: CEM (Central Electromagnetic Calorimeter), PEM (Plug Electromagnetic), CHA (Central Hadronic Calorimeter), WHA (Wall Hadronic) and PHA (Plug Hadronic). In addition, there are Forward Electromagnetic (FEM) and Hadronic (FHA) calorimeters. CDF Calorimeter system provides a full 2π coverage in ϕ , and in pseudorapidity η it covers region of up to 4.2. Rapidity coverage and segmentation of each of the calorimeter components are given in Table 4.2.

All calorimeter detectors are segmented into sets of towers pointing towards the center of the detector. Each tower consists of several layers of absorber (that forces the high energy particles to shower) and active medium (that collects the light produced by the showers that can be converted into the energy measurement). The CEM uses lead as the absorber, while CHA and WHA calorimeters use 4.5 interaction lengths of iron. All central and wall calorimeters use scintillator as the active medium. The components used in the study presented in this dissertation were CEM, CHA and WHA. The single particle

energy measurement resolution of the CEM is $13.7\%/\sqrt{E} \oplus 2\%$, for the CHA it varies with the angle but on average is $50\%/\sqrt{E} \oplus 3\%$, for the WHA it is $75\%/\sqrt{E} \oplus 4\%$. Jet energy resolution $\delta E_{jet}/E_{jet}$ of the calorimetry system in the central region is better than 11% for 30 GeV jets and improves to $\sim 7\%$ at higher jet energies (~ 100 GeV and above).

Table 3.2: CDF Calorimeter System coverage and detector segmentation in η - ϕ .

Central Calorimeter		
Name	Rapidity	η - ϕ segmentation
CEM	0.0 - 0.9	0.1 x 15
CHA	0.0 - 1.1	0.1 x 15
WHA	0.7 - 1.3	0.1 x 15
Forward Calorimeter Systems		
PEM	1.1 - 2.4	0.1 x 5
PHA	1.3 - 3.4	0.1 x 5
FEM	2.2 - 4.2	0.1 x 5
FHA	2.3 - 4.2	0.1 x 5

The plug and the forward-backward calorimeter systems use gas proportional chambers and were not used in the current analysis.

3.2.4 Other Sub-Detectors

In addition to the described above components that were directly used in this analysis, CDF has a number of other sub-systems that are important for a variety of experimental studies. Among them are: Muon System designed to register muons and,

using tracking information, determine their parameters, and Beam-Beam Counters used to estimate the luminosity by using coincidences of hits in the counters on two sides of the detector.

3.3 CDF Data Readout and Processing

For every bunch crossing, the full data is read out by the electronics of each of the components of the CDF detector. This data is written into the so-called Level 1 pipeline and is stored there until specially designed, fast (hardware implemented) algorithms determine whether this particular event is of any interest in terms of physics. If the decision is positive, a special signal (L1 Accept) is sent to the readout electronics by the Level 1 Trigger, and the data for this event is sent to the Level 2 pipeline. Simultaneously, a more thorough, and therefore slower, analysis of the data takes place. If the event is found to be sufficiently interesting, the Trigger sends a L2 Accept signal and all data banks from all CDF sub-detectors are read out. On Level 3, the data undergoes last check-ups to ensure that no information is lost or corrupt and the event gets written on disk or tape.

The data then is passed to the offline reconstruction package that converts the low-level data (hits in the chambers, raw amplitudes in the photo-multipliers etc.) into physically meaningful information (vertices, clusters of energy, tracks).

At CDF, the offline reconstruction package consists of several modules each responsible for particular type of measurement. The most important modules for this analysis were VXPRIIME, JETCLU, and TrackControl. VXPRIIME module uses the information from the vertex detectors to reconstruct the spatial position of the event

vertex (or vertices). JETCLU uses the calorimeter information and searches for clusters of energy deposited in the calorimeters and runs the jet algorithm to identify jets. TrackControl module is responsible for the tracking reconstruction. It uses the information from the CTC and (with default options) from the vertex detectors (VTPC and SVX) to find tracks and their parameters.

After running the production executable, the higher-level information is packed into banks and is written out in one of several adopted at CDF formats: the raw data, DST (semi-raw data) or PAD (high-level information). More complete information on the readout process, electronics specifications and the reconstruction procedure is published and available elsewhere [28].

In the analysis presented in this dissertation, the latest version 7.12 of the CDF offline production was used to re-process the DST data. The reason for not using the data in a PAD format was the need for a non-standard tracking reconstruction (no information other than from the CTC was used to identify tracks and determine their parameters). This was required to match the procedure of determining the CTC tracking inefficiencies, as discussed in the Appendix. Other modules were used in a standard configuration.

CHAPTER 4

DATA ANALYSIS TOOLS

Monte-Carlo generators have become indispensable tools in high-energy physics. Initially, the Monte-Carlo technique was invented to handle mathematical problems that would otherwise require complicated multi-dimensional integrations. Monte-Carlo technique has much faster convergence of the calculations and is indispensable for numerical calculations in many applications.

In high-energy physics, one often has to deal with complex problems involving hundreds of particles that cannot be handled by usual methods. A typical example is the simulation of a high-energy collision, in which often dozens of particles are produced flying with various energies and in all directions. Particle detectors, such as CDF, have different detection inefficiencies that vary depending on the kind of particle, its energy and many other parameters. Analytical calculation of this process, even if all parameters are known will be impossible. Monte-Carlo technique, in contrast, breaks the complex problems in steps and is capable of tracing every single particle as it passes through the detector experiencing various interactions, deflections etc.

4.1 Monte-Carlo Event Generators

Simulating a high energy processes using theoretical calculations that predict the probabilities of various kinds of interactions is the main purpose of Monte-Carlo generators. Comparison of real data to Monte-Carlo events simulated according to

particular theoretical predictions allows distinguishing between correct and incorrect theoretical predictions.

In practice, there are a number of calibrated and adjusted Monte-Carlo generators that incorporate accurate theoretical calculations and are used by experimentalists in the High Energy physics. Having a good event generator and a detector simulation program allows correcting the data for the detector inefficiencies in order to reconstruct true physical properties of particular processes.

Several event generators, such as JETSET [29], PYTHIA [30] and HERWIG [31], are widely used by experimentalists all over the world. Choice of the generator is usually determined by the kind of a physics problem at hand. For example, JETSET uses the so-called independent fragmentation model [32] to convert partons into hadrons and is definitely a bad choice for studies of the QCD color coherence effects. On the other hand, JETSET with its emphasis on the primary production process, proved to be very useful in exotic searches.

In this analysis, the Herwig 5.6 Monte-Carlo event generator was used. Herwig is a multi-purpose event generator that has a number of built-in processes. For QCD hard scattering, the dominant process in jet production, it uses Leading Order QCD calculations and has an option of linking different parton distribution function parameterizations (PDF).

With regard to the jet fragmentation, Herwig incorporates the knowledge of various color coherence effects, such as the Angular Ordering, and uses resummed Leading (Double) Log Approximation for the parton showering.

Hadronization in Herwig is done using the so-called cluster model of hadronization. This is implemented as follows: at some value of the transverse momentum, the branching stops, all gluons get split into pairs of quarks and anti-quarks. Then, the nearby quarks are grouped to create colorless clusters. Depending on the mass of the cluster, the cluster then either decays into final hadrons according to the available phase space or is forced to decay into smaller clusters, and those smaller clusters then decay into final hadrons. Very heavy unstable resonances are also forced to decay into lighter hadrons according to their decay modes and branching ratios.

Herwig is probably the most advanced generator in terms of handling the color coherence effects and this was the primary reason for choosing Herwig to estimate corrections that were applied to the data.

In general, the better the generator reproduces the data, the more reliable estimation of the necessary corrections can be obtained. Historically, Herwig was tuned and adjusted to reproduce data at LEP for e^+e^- collisions with the center-of-mass energy around the Z pole. The energies at the Tevatron are much higher than those at LEP, and possible imperfectness in Herwig, negligible at LEP, could grow into a serious discrepancy at the Tevatron energies. This makes it very important to make sure that the Monte-Carlo predictions are in agreement with the data. In Chapter 7, the CDF data is compared to Herwig and the implications of those comparisons are discussed.

4.2 Detector Simulation

Event generators, such as Herwig, generate the “physical” events, i.e. a list of particles and their momentum, with which they would leave the interaction point. In

practice, the data obtained in real experiments always suffers from detector inefficiencies and incomplete acceptances. As a result, a fraction of particles always escape undetected while those that are detected can be reconstructed with deviated parameters.

To reproduce actual distributions in the data, one has to additionally “smear” the predictions of the event generator to simulate the detector response. At CDF, a special package, called QFL [33], is used for these purposes.

QFL receives properly formatted data as a list of particles with corresponding parameters from a Monte-Carlo Event Generator and propagates them through the detector. While simulating the passage of the particles through the detector, QFL includes all appropriate effects, like multiple scattering of the particles, short-living particle decays, conversions in the material of the detector. It also reproduces the geometrical and instrumental inefficiencies of the detector. To properly compare the data with the Monte-Carlo simulations, one needs to use one of the event generators (Herwig in this study) and the QFL package to simulate the detector response.

CHAPTER 5

FEASIBILITY OF THE JET FRAGMENTATION STUDIES AT CDF

Although there is an obvious interest in performing jet fragmentation studies at a hadron machine such as the Tevatron, there are factors complicating the analysis as compared to the e^+e^- experiments that have to be properly accounted and appropriately corrected. First of all, the background environment is much less trivial because of the presence of the underlying event (the remnants of the original proton and anti-proton that participated in a hard scattering). Given the higher hadronic cross-sections, the probability of having more than one interaction in the same bunch crossing (secondary events often referred as the “pile-up”) is rather high. Incoming jet radiation needs to be properly subtracted. In hadron collisions, a part of the total energy, associated with the underlying event, always escapes the detector limiting the control of the jet energy measurement (in e^+e^- , one knows a priori the total energy that would be deposited in the calorimeter).

There are purely detector related factors, such as the tracking inefficiency, calorimeter response corrections and many others that are not unique for the hadron collider experiments, but are more complicated than at e^+e^- experiments. For example, the occupancy of the tracker is much higher, as compared to LEP, and inevitably leads to larger inefficiencies in tracking. This problem had to be specifically addressed in this analysis, and is discussed in detail in the Appendix.

As it was discussed previously, MLLA predicts the shape of the momentum distribution of particles in jets, their multiplicities, as well as differences in quark and gluon jets. Corresponding calculations predict a particular dynamics of these distributions as functions of the jet energy and the restricted cone around the jet, in which particles are counted. All these predictions can be verified experimentally, as well as the expected $E_{jet}\theta_c / Q_{eff}$ scaling of these predictions.

A possible program for a thorough investigation of how well MLLA agrees with the data, is:

- Extensive scan of the angular and jet energy dependencies of the particle properties in jets, by dividing data into sub-samples according to the jet energy and fitting distributions for particles falling into restricted cones of several sizes. Analysis of the distribution shapes should allow for extraction of the MLLA parameter Q_{eff} and serve as the consistency check of the MLLA.
- Measurement of the peak position of the momentum distribution for combinations of jet energies and the cone-sizes around the jet core. If plotted as a function of $E_{jet}\theta_c$, this would allow verification of the predicted by MLLA scaling $E_{jet}\theta_c / Q_{eff}$.
- The second constant, the normalization of the distribution K can be used to extract the LPHD parton-to-hadron conversion parameter K_{LPHD} and also the ratio of multiplicities in gluon and quark jets (the CDF data is a mix of gluon and quark jets).

- Inclusive multiplicity of particles in restricted cones around jets. This is a largely independent measurement of the same quantities. Experimentally, given that the MLLA parameters will not be required to follow the exact shape of the distributions only following the prescribed by MLLA energy evolution of the total multiplicity, such a measurement will represent additional cross-check on whether the possible coincidence is accidental or predetermined. The ratio of multiplicities, r , in gluon and quark jets and the LPHD parameter K_{LPHD} can be extracted as a result of this measurement.
- The parameter r has a well-defined model independent meaning. Given the model dependence of the parameters that could be extracted as described above, which is good for testing the MLLA self-consistency, it would be also interesting to compare these parameters with a model-independent measurements. One of the possible measurements is the comparison of the charged particle multiplicities in dijet data vs photon + jet data (enriched with quark jets) to extract the ratio r of multiplicities in gluon and quark jets.

The research program outlined in this section along with comparisons of the data to Herwig Monte-Carlo event generating program has been brought to realization at CDF and corresponding experimental results are presented in this dissertation.

CHAPTER 6

DATA SELECTION, CORRECTIONS AND ERROR ESTIMATES

In this section, the selection of the data sample is explained in detail along with the corrections that were applied to the data. Dominating contributions into the systematic uncertainty of the measurement are discussed, as well as techniques in estimating these uncertainties.

6.1 Data Selection and Quality Cuts

The analysis is based on the data collected in Run 1B (1993-1995) with total accumulated luminosity of $\sim 95 \text{ pb}^{-1}$. The 30, 50, 70 and 100 GeV jet E_T triggers were used, the first three were prescaled by the factors of 1000, 400 and 8, respectively.

Event selection was rather standard for CDF and can be summarized as follows:

- A “good” run was required (this means that all the sub-detectors and components of the CDF detector were functioning properly during the whole run, that typically lasted for 8-20 hours, depending on the lifetime of the beams);
- The allowed number of jets in the event was from 2 to 4 (third and fourth jets were allowed if soft to avoid a bias towards the narrow jets, as at sufficiently high energies a single astray track can be identified as a jet. For the lower dijet masses this requirement was insignificant);

- If there were three jets in the event, for the raw jet energies, the requirement was $E_T^{jet3} \leq 5\% \times (E_T^{jet1} + E_T^{jet2})$;
- If four jets: $E_T^{jet3} + E_T^{jet4} \leq 5\% \times (E_T^{jet1} + E_T^{jet2})$;
- For the two leading jets, it was additionally required that $|\eta^{jet1}| \leq 0.9, |\eta^{jet2}| \leq 0.9$ (this cut ensures that the jets fall into the central and the most robust part of the detector);
- The number of good vertices had to be no more than 2 (requiring only one vertex would significantly cut the statistics, allowing more than 2 vertices would introduce additional complications because of a larger number of tracks);
- The vertices had to be in the central region of CDF: $|z_v| \leq 60\text{ cm}$ (large displacement of the vertex affects the jet E_T measurement in the calorimeter and has larger probability of falling out of the central region of the CDF. Interactions were distributed around the center of the detector with a width of approximately 30 cm, so this cut was not very strict);
- In the case of two good vertices, sufficient spatial separation between the vertices was required: $|z_1 - z_2| \geq 10\text{ cm}$ (to avoid ambiguity with assigning tracks to a particular vertex).

After applying primary cuts, the energy of the jets was corrected, as discussed later in this chapter, and the following cuts were applied:

- Good balance (within the resolution of the calorimeter) of the two leading jets in transverse direction: $\left| \vec{E}_T^{jet1} + \vec{E}_T^{jet2} \right| \leq 15\% \times \left| E_T^{jet1} + E_T^{jet2} \right|$
- θ -angle of the dijet direction in the center-of-mass system was required to satisfy $45^\circ \leq \theta_{cm} \leq 135^\circ$ (otherwise, the complimentary cone subtraction discussed later could not be performed; only a negligible fraction of the events that have passed previous cuts were not satisfying this requirement)

Table 6.1: Bin-sizes and mean values for nine sub-samples of the dijet data.

Range of Dijet Masses (GeV/c ²)	Mean Dijet mass in the bin (GeV/c ²)
$072 < M_{jj} < 094$	$\langle M_{jj} \rangle = 81.86$
$094 < M_{jj} < 120$	$\langle M_{jj} \rangle = 104.27$
$120 < M_{jj} < 154$	$\langle M_{jj} \rangle = 129.98$
$154 < M_{jj} < 200$	$\langle M_{jj} \rangle = 166.99$
$200 < M_{jj} < 260$	$\langle M_{jj} \rangle = 217.36$
$260 < M_{jj} < 340$	$\langle M_{jj} \rangle = 282.99$
$340 < M_{jj} < 440$	$\langle M_{jj} \rangle = 365.31$
$440 < M_{jj} < 570$	$\langle M_{jj} \rangle = 472.54$
$570 < M_{jj} < 740$	$\langle M_{jj} \rangle = 600.45$

After all the cuts mentioned above were applied, the selected data sample had approximately 100,000 events. The data was further divided into bins according to the values of the dijet masses as shown in Table 6.1. The energies corresponding to the boundaries of the nearby dijet mass bins differed by a factor of ~ 1.3 in the dijet mass (further in the analysis, the size of the cones around the jet in which the particles were counted, was also varied by the same factor: $\theta_c = 0.17, 0.22, 0.28, 0.36, 0.47$). The factor

of 1.3 was chosen to be larger than the error of the dijet mass measurement $\delta M_{jj} / M_{jj} \sim 7-10\%$ due to the finite calorimeter energy resolution.

6.2 Corrections to the Data

The corrections that were applied account for physical effects as well as for the detector inefficiencies and non-linearities. They can be divided into two categories: jet corrections and track reconstruction corrections.

6.2.1 Jet Corrections

CDF defines jets using a cone algorithm defined in its Snowmass convention [34]; full details of its implementation at CDF can be found elsewhere [35]. The algorithm searches in cones of radius $R = \sqrt{(\Delta\phi)^2 + (\Delta\eta)^2} = 0.7$ around the calorimeter seed towers (any tower with the transverse energy E_T above 1 GeV) and adds towers with E_T above 0.1 GeV. If two or more adjacent towers are found within $R=0.7$, they are merged. The coordinates of the jet axis are calculated as weighted sums of the ϕ_i and η_i of towers assigned to the jet, the weights being proportional to E_{Ti} . Merging continues until a stable set of clusters is found.

The jet energy reconstruction has several effects, both physical and instrumental, that have to be properly corrected. First, there is the underlying event contribution, i.e. the deposition of energy in the calorimeter by the remnants of the initial proton and antiproton. Second, there is a contribution associated with the secondary interactions in

the same bunch crossing that also tends to increase the measured energy of the jet with respect to the true value. Third, some of the particles that actually belong to the jet are emitted under sufficiently large angles with respect to the jet axis. Their contribution can fall out of the cone in which the jet is defined. This effect tends to slightly decrease the measured energy of the jet and also needs to be accounted for.

In addition to physical effects, there are purely instrumental inefficiencies that also had to be corrected. First, the response of various towers of the calorimeter is non-homogeneous. Second, there are cracks between the towers of the calorimeter, and if the jet is pointing towards this crack the energy deposition will be smaller than if it were directed into the center of the tower. There are other effects, such as the non-linear response of the calorimeter as a function of the jet energy and the ratio of energy deposited in the electromagnetic and hadronic parts of the calorimeter.

These corrections are rather standard for various studies performed at CDF and are very well investigated. In this analysis, the standard JTC96S package was used to incorporate all required corrections to reconstruct the energy of the initial parent parton.

Another effect closely related to the jet energy measurement is the migration of events between the dijet mass bins. Given the jet energy resolution mentioned above (7-11 %), a jet's measured energy can fluctuate and be reconstructed with noticeably higher or lower energy. When the fluctuation is large, the whole event may be reconstructed with sufficiently higher dijet mass and fall into a wrong bin in the dijet mass. Then, taking into account that the dijet mass spectrum is close to a falling exponential, so that for any two adjacent bins the one to the left has much larger number of events, this smearing of the dijet mass spectrum results in average effective migration of the events to

the higher masses. Figure 6.1 shows the spectrum of dijet masses for a particular bin as reconstructed by the CDF detector (solid line) and the true (dashed line) dijet mass distribution. This plot was obtained by using Herwig 5.6 event generator and QFL detector simulation package.

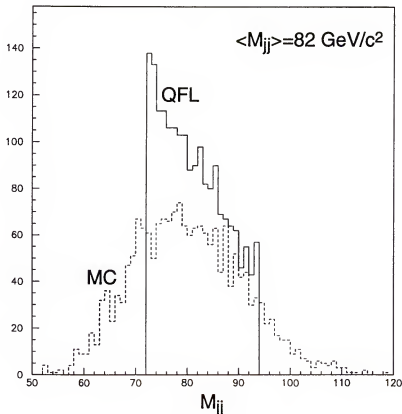


Figure 6.1: Example of the effects of the jet energy smearing. The solid line histogram corresponds to the dijet mass spectrum as reconstructed by the calorimeter (Monte-Carlo events were selected by the QFL), while the dashed line shows the true dijet mass distribution of the same events as obtained from the Herwig.

There are two ways to properly account for the migration effect. In the first case, the measured values are corrected based on the Monte-Carlo simulations (Herwig+QFL). This can be safely done if the Monte-Carlo generator reproduces the data well or the measured quantity is not very sensitive to the jet energy. In the second case, one has to

use the Monte-Carlo predicted spectrum of the dijet masses (that are reproduced well) for each particular bin when determining the mean values of the dijet mass. For the fits of the momentum distributions, the data has to be fitted using the theoretical prediction convoluted with the unsmearred dijet mass spectrum, and not the detector reconstructed one. Essentially, the difference between the two approaches is that in the first case one unsmears the data, and in the second one – the theory is getting smeared. In this study, for the mean multiplicity measurement the unsmearing was used, while for the fits of the momentum distribution the Monte-Carlo predicted dijet mass spectrum was used to convolute the theoretical predictions. Because of the logarithmic dependence of the results on the energy, these corrections were not large.

6.2.2 Tracking Corrections

Track parameters have been determined using tracking (CTC) information only. SVX vertex detector information was not used for tracking to avoid necessity of studying the SVX inefficiencies and, especially, effects related to how track hits linked between the CTC and SVX. Relevant track parameters were: the momentum of the track (determined from the curvature of the particle trajectory in the magnetic field), the azimuthal and radial direction of the particle flying from the interaction point. To distinguish particles originating in different vertices, two important parameters were used: dz , defined as $(z_{track} - z_{vertex})$, with the track z measured at the point of closest approach of the trajectory to the beam line, and the impact-parameter d defined as the minimal distance between the fitted trajectory of the particle and the beam-line.

Several corrections applied to the data dealt with the reconstruction of the individual particles inside the jets. The first correction applied was designed to compensate for the CTC tracking inefficiencies: tracks in high energy jets often overlap and cross each other resulting in losses or mismeasuring the parameters of particles. CTC inefficiency is a complicated issue. It proved to be very important for this analysis, and a special detailed study was performed to correctly account for this effect. The Appendix is entirely dedicated to the CTC tracking inefficiency correction estimation.

Then, there are several physical effects to be considered. First, there are a fraction of particles from the underlying event falling into the cone around the jet. Second, there are Tevatron induced backgrounds (beam losses), cosmics etc. To compensate for this effect, two “complementary” cones were defined: they were of the same size as the cones around the jet, in which particles were counted, and were located in the same way with respect to the beam line, but rotated so that they were at 90° with respect to the jet axis (i.e. as far as possible). This can be done as long as the θ -angle of the dijet direction in the center-of-mass system satisfies $45^\circ \leq |\theta_{cm}| \leq 135^\circ$. Thus defined cones statistically contain the same amount of the background tracks not associated with the jet, as the cones around jets. This allows subtracting the contribution of the uncorrelated background, as illustrated on Figure 6.2. This correction was found to be almost independent of energy, as one would expect.

Another contamination comes from the decays of K_S and the electrons produced in γ -conversions in the material of the detector. This contribution is correlated with the jet and cannot be removed by complementary cone subtraction. This effect was compensated by counting only tracks that were measured to originate in the primary vertex (by using

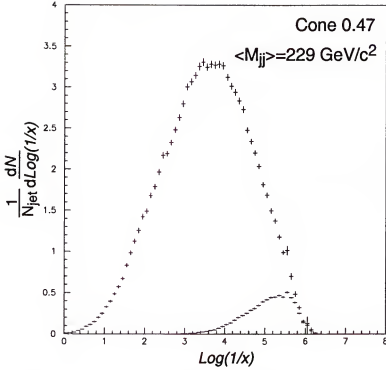


Figure 6.2: Complementary cone subtraction illustration. The upper histogram shows the corrected distribution, and the lower line shows the subtracted background contribution.

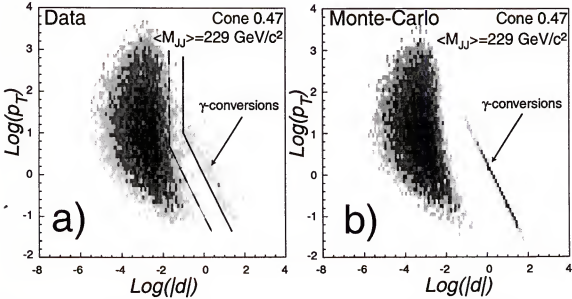


Figure 6.3: Distribution $\log(p_T)$ vs $\log(d)$ for tracks (after complementary cone subtraction). p_T is measured in GeV, d in cm.

appropriate vertex cuts, particularly the impact-parameter d). Figure 6.3 shows the distribution of $\log(p_T)$ vs $\log(d)$ after applying the complementary cone subtraction.

The impact parameter allows separating real particle tracks from those produced in conversions and decays. In the course of this analysis, it was found that a very clear separation of the conversion tracks can be found if one plots a distribution $\log(p_T)$ vs $\log(d)$. In this case, conversions produced at a certain radius appear as straight lines of negative slope with the intercept determined by the radius, at which the conversions occurred. In Figure 6.3 one can clearly see a concentration of tracks to the right of the main region. This concentration has a roughly linear shape and is due to the conversions. The source of the conversions was traced to the cables between the VTPC and the CTC. To exclude these backgrounds a cut was chosen as shown by a solid line on Figure 6.3a.

The dz cut was found to be not very important given that most of the backgrounds this cut is designed to handle were eliminated by the complementary cone subtraction. Still, to remove tracks coming from the neighboring vertex, the cut-off was chosen to be $|dz| < 6$.

For a cross-check, the QFL was additionally adjusted to match the resolution in determination of the impact parameter d , as measured in data, and it was verified that the cut-off parameters chosen result in a reasonable agreement between the Herwig+QFL with the conversions turned on and the original Herwig.

6.3 Systematic Uncertainties and Methods of Evaluation

Major sources of systematic errors can be listed as follows:

- Jet direction definition. Incorrect determination of the jet direction is especially dangerous for observables associated with the smaller cone-sizes around the jet axis.
- Jet energy determination systematic errors. The overall energy scale uncertainty (as much as 5%) and the uncertainties in the relative corrections associated with the calorimeter geometry affect the final measured parameters.
- Imprecise knowledge of the CTC efficiency correction. It affects most of the measured values.
- Choice of the track vertex cuts (impact-parameter d and dz). This choice affects how many valid, but mismeasured, tracks are rejected and how many irrelevant (background) tracks are included.
- For observables obtained from fitting the track momentum distributions, there is another systematic error: the choice of the fitting range. This is especially pronounced when a theoretical curve does not perfectly fit the data.

The fitting uncertainties are discussed in Chapter 7 where the fitting is described, and the procedure is explained in detail.

6.3.1 Systematics Associated with the Calorimetry

Incorrect definition of the jet direction (or, to be more precise, the direction of the parton that produced the jet) will result in incorrect assigning angles of tracks with

respect to the jet. Tracks, which are actually inside the cone, because of the incorrectly determined jet direction, may fall out of cone. Obviously, this effect should be larger for smaller cones and lower energies (at higher energies, jets are very narrow: thus, their direction is much better defined and, also, even if the jet direction is incorrect, vast majority of tracks still falls into the cone). We used Herwig in conjunction with QFL to check how significantly jet direction could be mismeasured. Figure 6.4 shows the angle between the true jet direction (parent parton direction as given by Herwig), and the direction obtained by QFL for three dijet mass bins with the average dijet masses $M_{jj}=82$, 229 and 628 GeV. As a crosscheck, the resolutions of the $\delta\varphi_{jj} = \varphi^{jet1} - \varphi^{jet2}$ distribution for the two opposite jets were measured and were found to be in a good agreement with the Herwig/QFL predictions.

To estimate the significance of this effect and to obtain a quantitative result for the corresponding systematic error, the jet direction in the data was additionally smeared using the obtained values of the angular resolutions. Thus obtained “second-order” affected distributions were fitted (in case of the quantities obtained from fits) and the results of the fits were compared to the original values. The difference between the nominal value of each observable and the deviated one was assigned as the systematic uncertainty.

Estimation of the uncertainties associated with the determination of the jet energy is rather straightforward and utilizes previous studies of the jet energy reconstruction, which resulted in the corrections used by JTC96S. Those corrections were obtained by fitting the actual calorimeter data to, for instance, the test-beam data. The uncertainties in the values of the corrections were estimated and built into JTC96S package. For the

“scale correction” (the other one is conventionally called “relative correction”), all data was reprocessed and re-binned by applying the JTC96S correction with energy scale shifted “up” and “down”. All observables were recalculated using deviated parametrizations, the largest difference with nominal values was considered as systematic uncertainty.

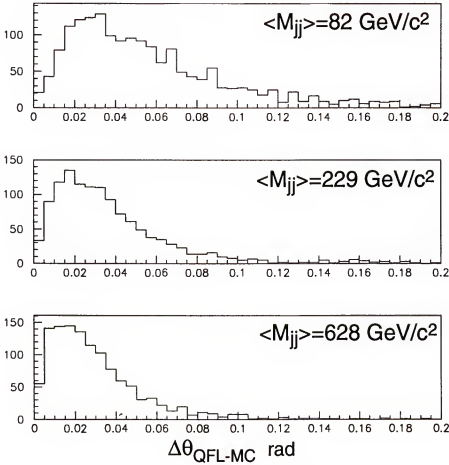


Figure 6.4: The angle between the true direction of the jet (extracted from Herwig Monte-Carlo) and the one reconstructed by the detector (QFL). One can see that the effect, as expected, is less significant for the higher dijet masses.

For the relative correction that compensates for cracks between the towers of the calorimeter and other geometry effects in jet energy determination, a similar approach

was used. In the past, the studies of the jet energy balancing (when the E_T of one jet is used as a reference and the second jet serves as a “probe” to see how the “probe” jet reconstructed energy depends on the jet direction) were performed to estimate the geometrical correction. There is a special option in JTC96S that determines whether the default or one of the two (upper and lower bound of the expected range of the correction value) deviated corrections is used. After reprocessing the data with deviated corrections, the results (parameters obtained from the fits of the distributions or the charged particle multiplicities) were compared to the originals obtained using nominal correction, and the difference was assigned as the systematical uncertainty. This effect was noticeably smaller than for the “scale” systematic error in the jet energy determination, as one could expect. Nevertheless, all systematic errors for each observable were calculated and included into the final uncertainties.

To evaluate the uncertainties due to the jet energy smearing, the detector resolutions in the QFL detector simulation package were adjusted to better match the data and the difference in observed values for the adjusted and the default case were taken as the systematic errors. With a relatively low scale of the correction, these uncertainties were estimated and found to be negligible.

In addition, the data was checked to have no biases with respect to the trigger thresholds due to selecting events with particular properties. Mean particle multiplicity as well as the charged energy fraction were used as the reference and no unexpected changes at the vicinity of the thresholds were found. Continuity of all measured values also suggests that the trigger effects did not affect the results.

6.3.2 Systematics Associated with the Tracking

The uncertainty in the CTC efficiency is a direct contribution to any tracking related measurements. The systematic effects in the CTC correction were evaluated and details can be found in the Appendix. To evaluate the effect of this uncertainty on the measured parameters, the CTC correction function was used in its nominal definition, and then with the deviated assumptions. All measured parameters were recalculated and the spread of the measured values was assigned as the systematic uncertainty.

To determine systematical uncertainty due to the vertex track cuts (impact-parameter d and dz), we investigated how the measured quantities (multiplicity, fitted parameters etc.) depended on possible variations in the vertex cuts. It was found that variation of the dz parameter had little effect. To conservatively estimate the effect of variations in the impact-parameter d , a stricter cut was applied to define the relevant tracks (dashed line on Figure 6.3 a). Effectively, this cut eliminated all tracks with a distance to the vertex position more than the CTC resolution uncertainties. Together with the nominal cut, this allows obtaining a conservative estimation of possible systematic errors related to the choice of cuts. The difference between the measured values for the default value of the cut-off and the deviated one was assigned as the uncertainty due to the choice of the vertex cuts. All parameters were calculated for the nominal choice and the deviated case. The change in the measured values was assigned as the corresponding systematic error.

CHAPTER 7

RESULTS AND COMPARISONS TO THE PREDICTIONS OF THE MODIFIED LEADING LOG APPROXIMATION (MLLA).

In this chapter, the main experimental results that were obtained in these studies are presented. The results can be grouped into three categories: measurement of the inclusive momentum distributions and multiplicities of charged particles in jets, model-independent measurement of the ratio of multiplicities in gluon and quark jets using photon + jet data, and comparisons of the properties of particles in jets to the predictions of Herwig Monte-Carlo.

The chapter is organized as follows. In the first section, the momentum distribution measurement is discussed, including the fit of the distributions with the MLLA limiting spectrum for the distribution normalization K and MLLA parameter Q_{eff} . Then, the distributions are fitted for the peak position to extract Q_{eff} and to verify the MLLA predicted $E_{jet} \sin \theta_c / Q_{eff}$ scaling. Next, the angular dependence of the normalization parameter K is discussed, and, finally, the LPHD parameter $K_{LPHD}^{charged}$ and the ratio r of multiplicities in a gluon and quark jets are extracted from K dependence on the jet mass. The second section is dedicated to the measurement of inclusive charged particle multiplicity, the extraction of the LPHD parameter $K_{LPHD}^{charged}$, and the ratio of multiplicities in gluon and quark jets r . The third section presents a model independent measurement of the ratio of charged particle multiplicities in gluon and quark jets using

the photon + one jet data. The fourth section presents comparisons of the data to Herwig Monte-Carlo. Discussion and conclusions are presented in the last section.

7.1 Measurement of the Momentum Distribution of Charged Particles in Jets.

Inclusive momentum distributions of charged particles in jets were measured for 9 available dijet mass sub-samples, and for three cone-sizes $\theta_c=0.28, 0.36$ and 0.47 .

The raw momentum distributions were corrected for effects discussed in Chapter 6. The order of applying these corrections is important and was as follows. First, the data was corrected for the contributions associated with γ -conversions, backgrounds and K^0, Λ decays by applying vertex cuts. Second, the CTC efficiency correction (see the Appendix for details) was applied. Then, the complementary cone subtraction was performed to eliminate the uncorrelated background tracks coming from the underlying event, multiple interactions in the same bunch crossing, Tevatron induced backgrounds, cosmics etc.

The final distributions were fitted with the MLLA limiting spectrum to extract the MLLA parameters, and, separately, for the peak position of the distribution to extract Q_{eff} . The fit procedure and the evaluation of the systematic uncertainties in the fitted parameters are discussed in the next sections.

7.1.1 Fits of the Distributions with the MLLA Limiting Spectrum.

Each of the 27 obtained distributions was fitted with the MLLA limiting spectrum function (Eq. 1.14) to extract the distribution normalization K , as well as the MLLA parameter Q_{eff} . The measured momentum distributions, along with the fit curves for the

largest cone of size $\theta_c=0.47$, are shown on Figure 7.1. The results of the fit can be found in Table 7.1.

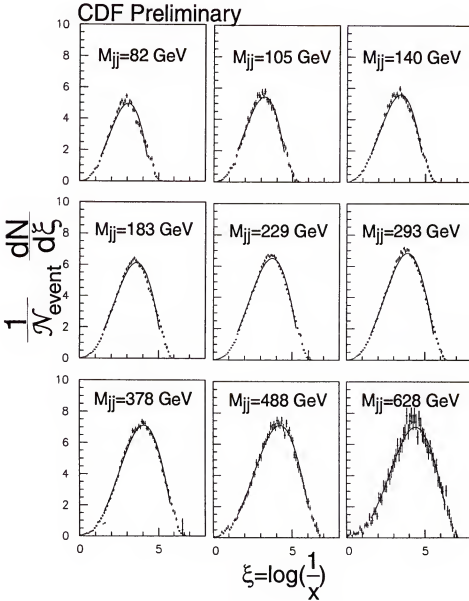


Figure 7.1: Evolution of the momentum distribution with energy for cone size 0.47. x is defined as p/E_{jet} (p is the particle momentum).

Table 7.1: Results of the fit of the data for all combinations of dijet masses and cone sizes. Data was fitted with classical MLLA gluon function. First uncertainty is the fit uncertainty in the fitted parameter for the default distributions, second – the systematic uncertainty. " χ^2 " corresponds to the fit with default corrections.

Dijet Mass GeV/c ²	Cone 0.28	Cone 0.36	Cone 0.47
82	$K=0.590\pm0.007\pm0.04$ $Q_{eff}=250\pm5\pm41$ $\chi^2/n.d.f.=85/21$	$K=0.632\pm0.005\pm0.04$ $Q_{eff}=262\pm5\pm45$ $\chi^2/n.d.f.=85/23$	$K=0.657\pm0.007\pm0.04$ $Q_{eff}=280\pm3\pm45$ $\chi^2/n.d.f.=128/26$
105	$K=0.596\pm0.007\pm0.03$ $Q_{eff}=247\pm1\pm41$ $\chi^2/n.d.f.=42/23$	$K=0.634\pm0.006\pm0.04$ $Q_{eff}=261\pm2\pm44$ $\chi^2/n.d.f.=47/26$	$K=0.649\pm0.008\pm0.03$ $Q_{eff}=279\pm1\pm44$ $\chi^2/n.d.f.=57/28$
140	$K=0.581\pm0.005\pm0.03$ $Q_{eff}=256\pm1\pm42$ $\chi^2/n.d.f.=95/26$	$K=0.592\pm0.005\pm0.03$ $Q_{eff}=247\pm1\pm42$ $\chi^2/n.d.f.=101/29$	$K=0.629\pm0.006\pm0.04$ $Q_{eff}=265\pm1\pm42$ $\chi^2/n.d.f.=86/31$
183	$K=0.560\pm0.004\pm0.03$ $Q_{eff}=237\pm3\pm39$ $\chi^2/n.d.f.=220/29$	$K=0.579\pm0.003\pm0.03$ $Q_{eff}=243\pm1\pm41$ $\chi^2/n.d.f.=229/31$	$K=0.598\pm0.005\pm0.03$ $Q_{eff}=260\pm3\pm41$ $\chi^2/n.d.f.=272/34$
229	$K=0.540\pm0.003\pm0.04$ $Q_{eff}=226\pm1\pm37$ $\chi^2/n.d.f.=175/31$	$K=0.561\pm0.003\pm0.04$ $Q_{eff}=236\pm1\pm40$ $\chi^2/n.d.f.=258/34$	$K=0.572\pm0.004\pm0.03$ $Q_{eff}=251\pm2\pm40$ $\chi^2/n.d.f.=230/36$
293	$K=0.536\pm0.004\pm0.03$ $Q_{eff}=230\pm3\pm38$ $\chi^2/n.d.f.=227/33$	$K=0.568\pm0.003\pm0.03$ $Q_{eff}=244\pm2\pm41$ $\chi^2/n.d.f.=182/36$	$K=0.586\pm0.004\pm0.03$ $Q_{eff}=250\pm2\pm40$ $\chi^2/n.d.f.=269/39$
378	$K=0.525\pm0.008\pm0.04$ $Q_{eff}=230\pm3\pm38$ $\chi^2/n.d.f.=130/36$	$K=0.535\pm0.005\pm0.03$ $Q_{eff}=227\pm2\pm39$ $\chi^2/n.d.f.=117/39$	$K=0.557\pm0.005\pm0.03$ $Q_{eff}=245\pm4\pm39$ $\chi^2/n.d.f.=118/41$
488	$K=0.484\pm0.006\pm0.03$ $Q_{eff}=212\pm4\pm35$ $\chi^2/n.d.f.=65/39$	$K=0.502\pm0.005\pm0.04$ $Q_{eff}=227\pm2\pm39$ $\chi^2/n.d.f.=73/41$	$K=0.513\pm0.007\pm0.03$ $Q_{eff}=241\pm5\pm38$ $\chi^2/n.d.f.=74/44$
628	$K=0.433\pm0.010\pm0.04$ $Q_{eff}=199\pm9\pm33$ $\chi^2/n.d.f.=82/41$	$K=0.448\pm0.009\pm0.04$ $Q_{eff}=206\pm9\pm35$ $\chi^2/n.d.f.=89/44$	$K=0.457\pm0.010\pm0.04$ $Q_{eff}=227\pm8\pm36$ $\chi^2/n.d.f.=83/46$

Uncertainties in the fitted parameters were obtained for the potential sources of the systematics that could have affected the measurement of the momentum distributions. Major sources of the systematic uncertainties were: the background track subtraction (vertex cuts), systematic uncertainty in the CTC efficiency measurement, and the

uncertainties associated with the jet energy and direction measurement. For each source of errors, the assumptions (cuts or the scales of the corrections) were varied to obtain a new distribution that was re-fitted for K and Q_{eff} as described in Chapter 6. New parameters were compared to their original values, and the differences were assigned as the corresponding systematic uncertainties in the fitted parameters.

In addition to the above listed uncertainties, there was another effect directly related to the fitting procedure, namely the choice of the fitting range. Momentum distributions have to be fitted only in a sufficiently soft part of the spectrum, in which the MLLA calculations are applicable (and, fortunately, where the absolute majority of the particles reside). However, this range is not strictly defined, and the somewhat arbitrary choice of the boundaries brings a new uncertainty into the fitted values of K and Q_{eff} . The nominal boundaries were defined as $\xi = 1.6$ and $\xi = \log(E_{jet} \times \sin\theta_c / 300 \text{ MeV})$. $\xi > 1.6$ corresponds to $x < 0.2$ and satisfies the limit $x \ll 1$, in which the MLLA calculations are performed. The right-hand border was chosen by requiring that particles should have transverse momentum $k_T \geq 300 \text{ MeV}$ (MLLA cannot describe partons with k_T lower than Q_{eff} and the fits suggested the Q_{eff} to be around 250 MeV).

To evaluate the corresponding uncertainty systematically, the fit boundaries were varied in such a way that in one case the spectrum was mostly following the left-hand side and the peak region of the measured momentum distribution, and in the second case the fit curve was forced to follow the right-hand side and the peak region of the measured distribution. In practice, it was achieved by shifting the right boundary to the left by 4 bins (2 bins for small cones) in one case, and shifting the left side boundary by the same amount to the right, in the other. Table 7.2 lists the contributions of individual systematic

uncertainties into the final error on the example of the fitted normalization of the distributions K for the cone of size 0.47. Note that the systematic errors associated with the variations of the fitting range were never dominating.

Table 7.2: Major uncertainties (in %) for the fitted parameter K , restricted cone 0.47. Systematic uncertainties of the same kind are strongly correlated bin-to-bin.

Dijet Mass	Fit range effects	CTC Efficiency	Vertex cuts	Jet Energy (scale)	Jet Energy (relative)
82	1%	1%	4%	3%	1%
105	1%	1%	3%	3%	1%
140	2%	1%	5%	3%	1%
183	2%	2%	4%	2%	1%
229	2%	2%	4%	3%	1%
293	3%	2%	4%	2%	1%
378	1%	3%	5%	1%	<1%
488	<1%	4%	5%	1%	<1%
628	1%	7%	6%	1%	1%

The results presented in Table 7.1 show the fitted parameters K and Q_{eff} as well as the uncertainties: first quoted uncertainty is the statistical error, while the second one includes all mentioned systematic uncertainties added in quadrature. The values of χ^2 do not include systematic effects and are referenced as they were obtained from the fit with the nominal corrections.

There are several observations to be made before proceeding further. Quantitatively, the fit is far from being perfect: the χ^2 values are high and one can see a clear, though small, excess of data over the MLLA prediction to the left of the peak. This indicates that MLLA cannot be considered as an ultimate all-describing model. At the same time, the qualitative agreement is very good, showing sufficiently high level of consistency between the theory and the data. This is especially important given the fact

that theory has almost no handles for tuning, as the shape of the distribution (e.g. the peak position and the width) are fully determined, for all masses and cone sizes, by a single parameter Q_{eff} . Detailed discussion of the parameter K is presented in sections 7.1.4 and 7.1.5.

7.1.2 Q_{eff} from the MLLA Fit

For the MLLA to be consistent with the data, parameter Q_{eff} has to be constant for all combinations of dijet masses and cone-sizes. Figure 7.2 shows the scan of the values of Q_{eff} as a function of the dijet mass for the three cone-sizes.

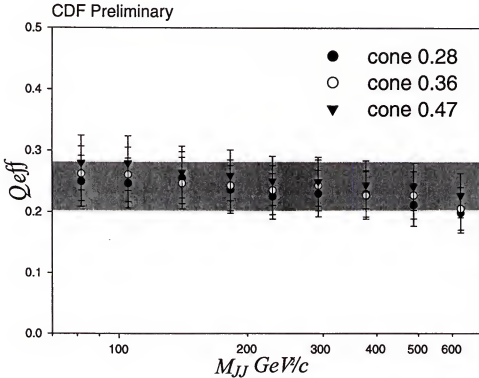


Figure 7.2: Fitted values of the parameter Q_{eff} obtained from the inclusive momentum distributions of charged particles in jets for nine dijet mass bins and three cone-sizes $\theta_c=0.28, 0.36$ and 0.47 .

Clearly, there are trends not predicted by the MLLA: Q_{eff} tends to get smaller for larger energies and smaller cones (systematic uncertainties are correlated and cannot account for these trends). However, these deviations are moderate over a large range of energies, and could be due to the higher order effects and naïve assumption of one-to-one parton-hadron correspondence about the hadronization. From Table 7.1 and Figure 7.2 the reported value for the Q_{eff} is 240 ± 40 MeV, where 40 MeV represents the scale of the variations in the measured value of Q_{eff} as well as the range of the systematic uncertainties.

7.1.3 Fit for the Peak Position of the Distributions. MLLA Scaling. Extraction of Q_{eff}

According to Eq. (1.3), the peak position of the momentum distribution is predicted to depend only on parameter Q_{eff} and to be independent of the normalization K . The distributions obtained as described in the previous section were fitted for the peak position with a regular gaussian. This measurement is somewhat different from the one based on the fitting the data with the limiting spectrum because the measurement of the peak position is decoupled from the width of the distribution.

The study of the systematic uncertainties was performed in the exact same way as when fitting the distributions with the MLLA limiting spectrum. The uncertainties associated with the fit range were smaller in the case of the peak measurement, as in this case there is no problem associated with the fitting function not fully reproducing the data. Table 7.3 presents the results of the fit of the peak position for different cone sizes along with statistical and systematic errors.

Table 7.3: Results of the fit of the data for the peak position of the momentum distribution. All combinations of dijet masses and cone sizes. The first uncertainty is the uncertainty in the fitted parameter for the default distributions, and the second one is the sum of all systematic uncertainties added in quadrature.

Dijet Mass GeV/c ²	Cone 0.28	Cone 0.36	Cone 0.47
82	2.63±0.02±0.09	2.78±0.01±0.11	2.90±0.01±0.09
105	2.84±0.02±0.09	2.97±0.02±0.12	3.07±0.01±0.09
140	2.99±0.01±0.10	3.13±0.01±0.13	3.25±0.01±0.10
183	3.19±0.01±0.11	3.31±0.01±0.13	3.44±0.01±0.10
229	3.35±0.01±0.11	3.49±0.01±0.14	3.60±0.01±0.11
293	3.49±0.01±0.12	3.62±0.01±0.15	3.72±0.01±0.11
378	3.65±0.01±0.12	3.82±0.02±0.15	3.91±0.01±0.12
488	3.88±0.02±0.13	4.00±0.02±0.16	4.10±0.02±0.12
628	4.05±0.04±0.13	4.18±0.04±0.17	4.31±0.03±0.13

An important verification of the consistency of the MLLA with the data can be performed using this measurement. Eq. (1.3) shows that the peak position of the distribution depends not just on Q_{eff} but on a combination of parameters, namely $E_{jet} \sin\theta_c/Q_{eff}$, i.e. the theory predicts a clear and verifiable scaling of the data on $E_{jet} \sin\theta_c/Q_{eff}$.

Figure 7.3 shows the evolution of the peak position as a function of $M_{jj}\sin\theta_c$. The data unambiguously agrees with the MLLA prediction. For illustration purposes, the data from $e+e-$ and ep experiments [36] is also shown on the same plot and is in agreement with the CDF measurement. A fit of the CDF data yields $Q_{eff} = 256 \pm 13$ MeV in agreement with the result of the previous section. For comparison, the predictions of the Leading Log Approximation and the fragmentation without color coherence (both models predict the slope of the corresponding lines) are shown and are clearly not supported by data.

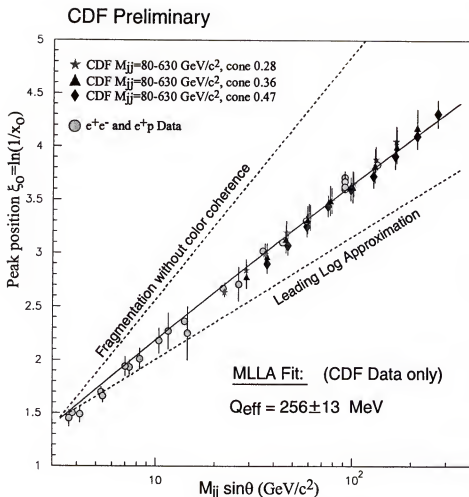


Figure 7.3: Peak position of the inclusive momentum distributions plotted against $M_{jj} \sin\theta_c$ (θ_c - opening angle). The MLLA fit gives $Q_{eff} = 256 \pm 13 \text{ MeV}$.

7.1.4 Dependence of the Fitted Parameter K on the Size of the Cone

Figure 7.4 shows the momentum distributions and the fit results for the three cone-sizes and a fixed dijet mass $378 \text{ GeV}/c^2$. According to Eq. (1.15), the parameter K , being a function of the jet energy, does not depend on the cone size in which particles are counted. From Table 7.1 one can see that, indeed, K remains fairly constant. However, a

more closer look shows that this is not completely true: there is a small trend of K getting smaller for smaller cones.

Note that the variations in K are not very large: the change in K is of the order of 6% while the height of the distribution changes by 20%. Also, it was found that refitting all available data together with one single Q_{eff} makes these variations all but disappear.

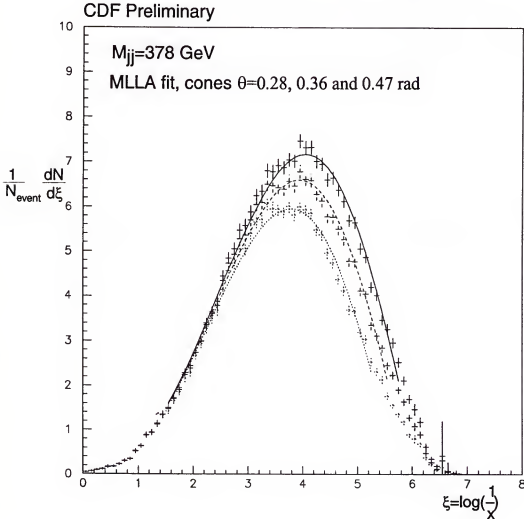


Figure 7.4: Fitted inclusive momentum distributions for dijet mass 365 GeV for 3 available cone sizes.

7.1.5 Extraction of the LPHD Parameter $K_{LPHD}^{charged}$ and the Ratio of Multiplicities in Gluon and Quark Jets r

According to Eq. (1.15), extraction of the parameters r and $K_{LPHD}^{charged}$ requires knowledge of the quark and gluon fractions in the data sample. These fractions depend on the jet energy and are determined by the dynamics of the hard scattering and the parton distribution functions (PDF), which determine the quark and gluon content in the original colliding particles, protons and antiprotons.

These fractions can be extracted sufficiently reliably using the Herwig Monte-Carlo and the detector simulation. The jets in the data used in this study were produced in the Leading Order QCD hard scattering (jet energy balance requirement explicitly suppresses NLO contributions), and the LO QCD is properly implemented in Herwig. Regarding the PDFs, these are known sufficiently well at the values of x relevant to this analysis. To estimate the systematic uncertainty, one can use different existing parametrizations of PDF and compare the results.

To ensure that events in the Monte-Carlo are selected in exact same way as in the data, the QFL detector simulation package was used, and the event selection was performed with the same cuts as in the data. Fig 7.5 shows how the gluon jet fraction changes as a function of the dijet mass for several choices of PDFs: CTEQ4M [37] (used as the default), CTE4HJ [38] (increased gluon content at high x). For comparison, an old, but standard for Herwig, Duke-Owens 1.1 parametrization [39] is also shown.

Eq. (1.15) predicts that K should depend linearly on the gluon jet fraction in the dijet mass bins, and a linear fit of the data allows extracting r and $K_{LPHD}^{charged}$ (in

combination with the theoretical next-to-MLLA correction factor F_{nMLLA} , see Chapter 1). Figure 7.6 shows the values of the parameter K as a function of the gluon content in 9 dijet mass bins, for the largest cone-size $\theta_c=0.47$.

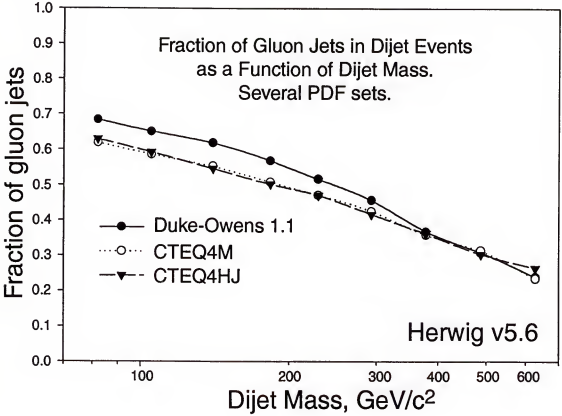


Figure 7.5: The evolution of the gluon jet fraction in the dijet mass bins as a function of the mean dijet mass in the bin.

The data was fitted for parameters, and the fit yielded $K_{LPHD}^{charged}=0.58\pm0.11$ (assuming $F_{nMLLA}=1.3\pm0.2$, see the discussion of the next-to-MLLA corrections in Chapter 1), and $r=1.8\pm0.4$. The fit took into account the correlations of the systematic uncertainties of the same kind between the data points. The degree of correlations was varied to estimate the sensitivity of the result to this unknown parameter, and the range of

variations in the fitted values was added to the systematic uncertainty of the measurement.

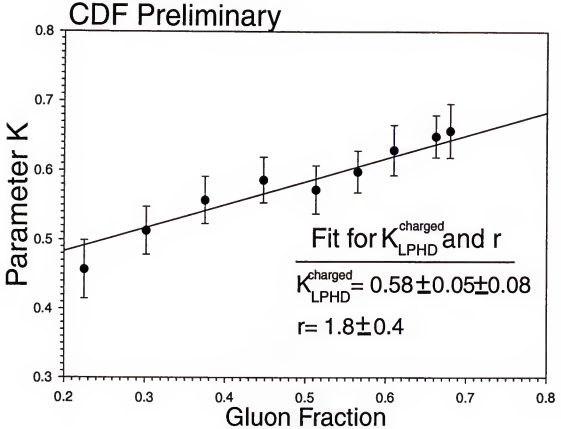


Figure 7.6: Evolution of the parameter K as a function of the gluon jet fraction in the dijet samples. Cone 0.47. Gluon fractions were extracted using Herwig 5.6 Monte-Carlo and detector simulation.

7.1.6 Summary

The momentum distribution of charged particles in jets follows the predictions of the Modified Leading Log Approximation well for a large range of jet energies and several cone-sizes. Quantitative disagreement, such as the high χ^2 values of the fits of the momentum distribution, indicates presence of other effects, not described by MLLA.

These effects could be due to higher order (with respect to MLLA) corrections and hadronization effects (remember that LPHD is clearly too naïve to be true in all details). We report the measured MLLA cut-off parameter Q_{eff} to be 240 ± 40 MeV (256 ± 13 MeV based on the peak position). LPHD parton-to-hadron conversion rate $K_{LPHD}^{charged} = 0.58 \pm 0.11$, and the ratio of multiplicities in quark and gluon jets $r = 1.8 \pm 0.4$. The MLLA suggested $E_{jet} \sin \theta_c / Q_{eff}$ scaling is verified for the first time and is supported by data.

7.2 Measurement of the Inclusive Charged Particle Multiplicity. Comparisons to the MLLA Predictions. Extraction of the Ratio r and LPHD Parameter $K_{LPHD}^{charged}$

Charged particle multiplicities were obtained for tracks falling into three restricted cones with $\theta_c = 0.17, 0.28$ and 0.47 around the jet axis. All multiplicities quoted below are per jet. To reconstruct the true charged particle multiplicities from the raw data, the same cuts and corrections as in the case of momentum distributions had to be applied.

Additionally, a small fraction of tracks coming from γ -conversions and decays that were not removed by the vertex cuts had to be subtracted. The Herwig 5.6 Monte-Carlo was used to evaluate the number of the remaining contamination. QFL detector simulation package has the option of turning these effects on and off. Two Monte-Carlo samples were generated to compare the multiplicity and to estimate this effect. The scale of this correction was 0.3 (0.8) tracks per jet for the lowest (highest) dijet mass data samples (for cone size $\theta_c = 0.47$).

Also, the effect of the event migration related to the jet energy resolution was handled differently than for the momentum distributions. As it was mentioned in Chapter

6, the exponential form of the dijet mass distribution results in the fact that each dijet mass bin always has an adjacent bin to the left with much higher number of events than the bin to the right. Because of the finite jet energy resolution, events are routinely getting reconstructed with higher or lower energy than they really have and occasionally fall into a wrong bin.

To estimate the scale of the migration effect and corresponding correction, the Herwig Monte-Carlo together with the QFL detector simulation were used. To simulate the migration, nine large Monte-Carlo samples (one for each dijet mass bin) were produced. The multiplicity was calculated first when the events in the bin were selected according to the “true” dijet mass energy (i.e. the di-parton mass taken from Herwig) and, second, when events were selected by the QFL detector simulation package. Relative correction was calculated as the ratio of the two measured multiplicities. This estimation is reliable given that Herwig reproduces the slope of the multiplicity as a function of energy well (see the section of this Chapter dedicated to the Herwig comparisons). Associated systematic uncertainty was estimated by varying the detector resolution in QFL and was found to be negligibly small.

Other systematic uncertainties were estimated in a standard manner. Major sources of systematic uncertainties and their contributions into the final systematic uncertainty for the example of the multiplicity in the cone 0.47 are listed in Table 7.4.

Table 7.5 summarizes the multiplicities for three jet opening angles and all dijet mass data samples. One has to remember that the uncertainties from a given source are strongly correlated between different dijet mass samples and such correlations have to be properly taken into account in the data analysis.

Table 7.4: Major uncertainties for charged track multiplicity in dijet events for a restricted cone 0.47. Systematics are believed to be strongly correlated.

Dijet Mass	Multiplicity	Stat Error	CTC Efficiency	Vertex cuts	Jet Energy (total)	Total Syst error
82	12.3	0.1	0.2	0.9	0.4	1.0
105	13.8	0.1	0.2	1.0	0.4	1.1
140	15.0	0.1	0.2	1.0	0.4	1.1
183	17.4	0.1	0.3	1.1	0.4	1.3
229	18.8	0.1	0.4	1.2	0.3	1.3
293	20.6	0.1	0.5	1.4	0.3	1.5
378	22.7	0.2	0.8	1.9	0.1	2.0
488	24.3	0.2	1.0	1.8	0.1	2.0
628	25.0	0.4	1.4	2.1	0.5	2.5

Table 7.5: Measured values of inclusive charged particle multiplicity per jet for tracks falling into restricted cones with opening angles $\theta_c=0.17, 0.28$ and 0.47 . The first error is statistical and the second one is the total systematic uncertainty. Systematic uncertainties are strongly correlated.

Dijet Mass GeV/c^2	N_{events}	Cone 0.17	Cone 0.28	Cone 0.47
82	4,148	$2.9 \pm 0.0 \pm 0.2$	$4.5 \pm 0.0 \pm 0.3$	$6.1 \pm 0.0 \pm 0.5$
105	1,968	$3.4 \pm 0.1 \pm 0.3$	$5.1 \pm 0.1 \pm 0.4$	$6.9 \pm 0.1 \pm 0.5$
140	3,378	$4.0 \pm 0.0 \pm 0.3$	$5.8 \pm 0.1 \pm 0.4$	$7.5 \pm 0.0 \pm 0.6$
183	12,058	$4.9 \pm 0.0 \pm 0.3$	$6.8 \pm 0.0 \pm 0.4$	$8.7 \pm 0.0 \pm 0.6$
229	31,406	$5.2 \pm 0.0 \pm 0.4$	$7.3 \pm 0.0 \pm 0.5$	$9.4 \pm 0.1 \pm 0.6$
293	23,206	$6.0 \pm 0.1 \pm 0.4$	$8.2 \pm 0.2 \pm 0.5$	$10.3 \pm 0.1 \pm 0.7$
378	7,153	$6.7 \pm 0.1 \pm 0.5$	$8.9 \pm 0.2 \pm 0.7$	$11.3 \pm 0.1 \pm 1.0$
488	1,943	$7.4 \pm 0.1 \pm 0.6$	$9.7 \pm 0.2 \pm 0.8$	$12.2 \pm 0.1 \pm 1.0$
628	416	$7.5 \pm 0.2 \pm 0.7$	$9.9 \pm 0.2 \pm 0.9$	$12.5 \pm 0.2 \pm 1.3$

Figure 7.8 presents a plot of multiplicity for the largest available cone $\theta_c=0.47$ compared to predictions of MLLA corresponding to different values of the ratio of gluon and quark multiplicities r . The set of smooth lines corresponds to r running from 1 (upper curve) to $r=9/4$ (classic MLLA, lower curve). The plot makes it visually evident that the most likely value of r is between 1.4 and 2.0.

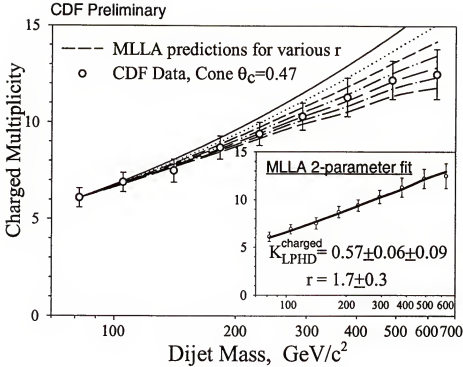


Figure 7.7: Mean charged multiplicity for the largest available cone $\theta_c=0.47$ compared to predictions of MLLA corresponding to different values of r - ratio of gluon and quark multiplicities. The set of smooth lines corresponds to r running from 1 (upper curve) to $r=9/4$ (classic MLLA, lower curve).

The model has two parameters: Q_{eff} and $K_{LPHD}^{\text{charged}}$, and the presence of quark and gluon jets brings the third one - r . However, due to correlations between Q_{eff} and $K_{LPHD}^{\text{charged}}$, average multiplicity measurements alone do not allow the extraction of all three parameters, Q_{eff} , r and $K_{LPHD}^{\text{charged}}$. Therefore, Q_{eff} was fixed at 240 MeV, as obtained from the fits of momentum distributions, and the data was fitted with the function (1.13) for two parameters: r and the combination $K_{LPHD}^{\text{charged}} \times F_{nMLLA}$.

Fit yielded the following results: $r=1.7 \pm 0.3 \pm 0.0 \pm 0.0$ for the ratio of multiplicities and $K_{LPHD}^{\text{charged}} \times F_{nMLLA} = 0.74 \pm 0.04 \pm 0.06 \pm 0.04$. The first uncertainty comes from the

statistical and systematic experimental errors, the second one from variations of Q_{eff} by ± 40 MeV, and the third one from using different PDFs. Apparently, the choice of Q_{eff} and PDF had little effect on the measurement of r . Assuming, as before, $F_{nMLLA}=1.30\pm 0.20$, the data yielded $K_{LPHD}^{charged}=0.57\pm 0.06\pm 0.09$. The first uncertainty includes all statistical and systematic uncertainties discussed above, while the second one comes from the theoretical uncertainty in F_{nMLLA} .

In summary, the mean inclusive charged particle multiplicities in dijet events, for a range of dijet masses and three cone-sizes, were measured. The data was compared to calculations carried out in the framework of the Modified Leading Log Approximation complemented with the hypothesis of the Local Parton-Hadron Duality. Assuming that multiplicity evolves with the energy as prescribed by the MLLA, the ratio of parton multiplicities in gluon and quark jets $r = N_{gluon}^{parton} / N_{quark}^{parton}$ was measured to be 1.7 ± 0.3 and the LPHD parton-to-hadron conversion constant $K_{LPHD}^{charged}$ to be 0.57 ± 0.11 .

7.3 Comparison of the Photon+Jet and the Dijet Data. Model-independent Measurement of the Ratio of Multiplicities in Gluon and Quark Jets r .

So far, the results on the ratio of multiplicities in gluon and quark jets were extracted in the context of MLLA, i.e. the measurement of r obtained above has strong model dependence. At the same time r , being the ratio of multiplicities in gluon and quark jets, has a well-defined model-independent meaning. It is interesting to compare the previously found value of r to a model-independent measurement. One of the ways to perform such a measurement is to compare the inclusive charged multiplicity for two

samples with different fractions of quark and gluon jets in them. Dijet data from the lower energy bins is enriched with gluon jets (see Figure 7.5). One of the possible choices for the second data sample, enriched with quark jets is the photon + one jet data (as photon does not couple to the gluon, the gluon jets are suppressed).

The photon + jet data selection was very similar to the one used for the dijet data. The photons were selected by requiring a single electromagnetic cluster with almost no energy deposit around it and no CTC tracks in a cone of size 0.4 around the photon candidate direction. The fraction of real photons was determined using the efficiencies of the photon conversions in the CPR that allowed events with one photon to be statistically distinguished from the events with a neutral pion decaying into two photons – the major background.

The photon + jet data was binned according to the photon+jet invariant mass in the same way as for the dijets. The lower cross-section of the photon+jet production limited the analysis to the comparison of the two data samples for the three lowest energy bins only.

The inclusive charged particle multiplicity in the jet opposite to the photon candidate was calculated and compared to the multiplicity in the jets coming from the dijet data. Uncorrected multiplicities for both samples are shown in Table 7.6. The fraction of the quark jets in the pure photon+jet sample were estimated from the Herwig Monte-Carlo in the same way as for the dijet data. The fraction of the gluon and quark jets among the fake photon (neutral pions in a low multiplicity jets) + jet data was also determined using Herwig. Table 7.7 shows these fractions.

The ratio of multiplicities in gluon and quark jets r was calculated and can be found in Table 7.8. Figure 7.8 shows the dependence of r on the jet energy.

The measured ratios for the three jet energies are consistent with the expectation of r being a weak function of energy. The model independent result obtained in this section is in a good agreement with the ratio measured in the context of MLLA.

Table 7.6: Inclusive charged multiplicity in dijet and γ -jet samples. CTC corrections are not applied. Uncertainties are statistical only.

Mean Jet Energy	Jet-Jet Multiplicity	Photon-Jet Multiplicity
40 GeV	5.77 ± 0.03	4.80 ± 0.05
53 GeV	6.48 ± 0.05	5.59 ± 0.08
67 GeV	7.18 ± 0.03	6.19 ± 0.14

Table 7.7: Comparative properties of the dijet and γ -jet samples. The first uncertainty in the fraction of real photons in the γ -jet sample is the statistical uncertainty of using the CPR method, while the second one is the systematical error.

Mean Jet Energy	Fraction of real photons in γ -jet	Fraction of gluon jets in dijets	Fraction of gluon jets in pure γ -jet
40 GeV	$0.72 \pm 0.05 \pm 0.05$	0.62 ± 0.03	0.16 ± 0.02
53 GeV	$0.89 \pm 0.08 \pm 0.06$	0.59 ± 0.02	0.24 ± 0.03
67 GeV	$0.96 \pm 0.12 \pm 0.07$	0.56 ± 0.03	0.26 ± 0.03

Table 7.8: Measured ratio of multiplicities in gluon and quark jets. The first uncertainty is statistical and the second one is systematical.

Range	$\langle E_{\text{jet}} \rangle$	Ratio $r = N_{\text{gluon}}/N_{\text{quark}}$
$36 < E_{\text{jet}} < 47$	40 GeV	$1.76 \pm 0.11 \pm 0.15$
$47 < E_{\text{jet}} < 60$	53 GeV	$1.59 \pm 0.12 \pm 0.10$
$60 < E_{\text{jet}} < 77$	67 GeV	$1.65 \pm 0.20 \pm 0.24$

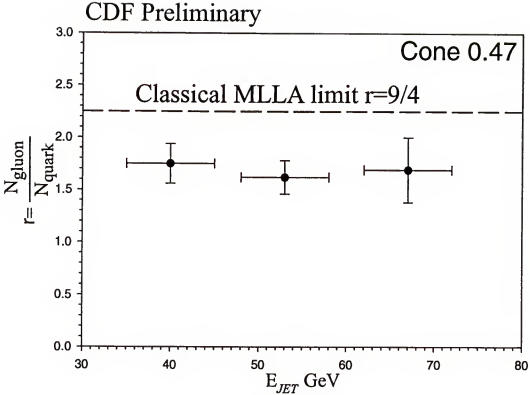


Figure 7.8: Measured ratio of charged particle multiplicity in gluon and quark jets. Statistical and systematical errors added in quadrature.

7.4 Particle Properties in Jets and Comparisons to Herwig Monte-Carlo

In general, the use of the Herwig Monte-Carlo could be unsafe for estimation of corrections and systematic uncertainties in the measurements presented above. This would be the case, if the Monte-Carlo were not well reproducing the data. As it was mentioned in Chapter 2, Herwig uses resummed perturbative calculations similar to MLLA for parton branching, and the cluster model of hadronization. However, it was tuned to reproduce the data at LEP for center-of-mass energies around the Z-pole. No special tune-ups were ever made to Herwig to reproduce the data at the Tevatron. Given

that the energies at the Tevatron are much higher than those at LEP, it is important to make sure that, after expanding towards larger energies, Herwig is still in agreement with data. Should a discrepancy between data and Herwig be found, it would complicate estimation of the corrections and systematic uncertainties and make Herwig Monte-Carlo unusable for describing particles in jets.

To make sure that such use is justified, a series of measurements were performed and the results were compared to the predictions of Herwig (plus the detector simulations).

7.4.1 Mean Charged Multiplicity

Figure 7.9 shows how the average charged particle multiplicity in three restricted cone-sizes changes with M_{jj} and how it compares to Herwig Monte Carlo. The error bars are statistical and systematic uncertainties added in quadrature. Herwig predictions on Figure 7.9 were scaled by a factor 0.89 to follow the data, as it was found that Herwig predictions were systematically higher than the data points.

Normalizing Herwig by a constant brings data and Monte-Carlo predictions closer. The data was fitted with Herwig, assuming that the normalization is a free parameter. The fit was done separately for the three data sets corresponding to the three cone sizes, and the results can be found in Table 7.10.

Fit results suggest that an additional normalization is preferred, and the desired scale factor was $N=0.89\pm0.06$. From this measurement alone, the discrepancy is only a 2σ effect and it is not possible to determine whether the Herwig simply overestimates the total multiplicity or it fails to reproduce more properties of the particle in jets on a more

fundamental level. Further studies have shown that simple normalization is sufficient, but the level of the discrepancy in the normalization is more significant than what comes out of the multiplicity measurement.

Table 7.10: Results of the fit of the Herwig to data for the Herwig overall normalization of the multiplicity along with corresponding values of χ^2 . Normalization was assumed to be a free parameter.

	Cone 0.17	Cone 0.28	Cone 0.47
N	0.89 ± 0.06	0.89 ± 0.06	0.88 ± 0.05
χ^2 / ndf	11.02/8	6.69/8	3.88/8

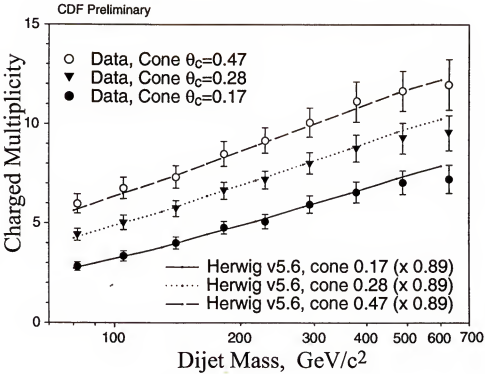


Figure 7.9: The average charged particle multiplicity in three restricted cone-sizes changes with M_{jj} and how it compares to Herwig Monte Carlo.

7.4.2 $dN/d(k_T)$ Distribution

The scatter plot of $d^2N/dk_T d\theta_c$ for $M_{jj}=230$ GeV (Figure 7.10) clearly shows that tracks tend to pile up at very low k_T values (k_T is the transverse particle momentum with respect to the jet axis, θ_c is the angle between the jet direction and the particle).

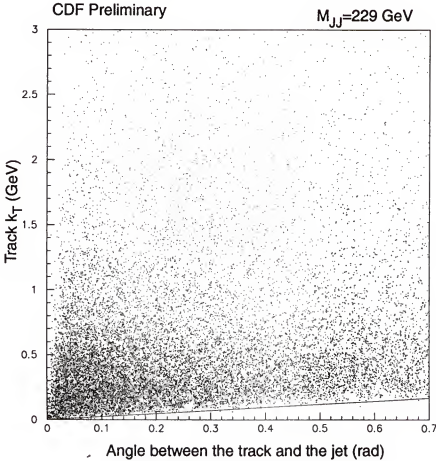


Figure 7.10: Scatter plot of the track transverse (with respect to the jet) momentum vs angle between the track and the jet direction.

The triangular void at the bottom corresponds to the CTC track reconstruction efficiency falling to zero for tracks with $p_T \leq 300$ MeV (p_T is the momentum of particle in the plane transverse to the beam-line and transverse to the direction of the magnetic field

in the tracker). At lower momenta, tracks start looping inside the tracker. The line on the plot corresponds to $k_T = p_{Tmin} \times \sin\theta_c = (300 \text{ MeV}) \times \sin\theta_c$ and is intended to indicate where most of the tracks are being lost and no efficiency corrections can be applied to recover for such losses. One may also notice a smaller gap along the vertical axis. This one is quite physical: it corresponds to tracks with momenta close to the jet energy, where the available phase space collapses. The main purpose of this plot is to indicate where the unrecoverable CTC losses happen so that one could correctly interpret the next figure.

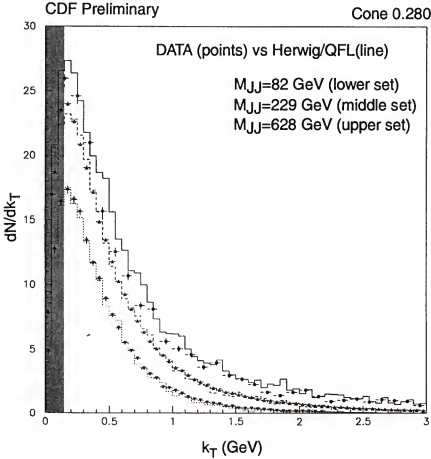


Figure 7.11: Distribution of tracks as a function of the track transverse (with respect to the jet direction) momentum.

Figure 7.11 shows the dN/dk_T distributions for 3 different dijet masses together with the Herwig/QFL Monte Carlo. The cone size is $\theta_c = 0.28$ and, as seen from Figure 7.10, tracks with k_T above 150 MeV are trustworthy. Besides the fact that it is scaled by a factor of 0.89, Herwig (plus the detector simulation) reproduces data very well over a wide range of k_T from ~ 150 MeV to a few GeV. Also note, that the origins of the uncertainties for the high and low k_T regions are very different. Therefore, it is very unlikely that systematic uncertainties could make the measurement consistently lower by 11% over the whole range of measured k_T .

7.4.3 $dN/d(\log p)$ Momentum Distribution

The $dN/d\log(p)$ distribution is essentially the same as the $dN/d\xi$ spectrum studies previously. Figure 7.12, apart from showing a good agreement with Herwig Monte-Carlo, also emphasizes an interesting feature: the multiplicity grows mostly due to the partons with higher and higher momenta and flying out at smaller and smaller angles, while the soft part remains practically unchanged.

This effect is a direct consequence of the color interference. To understand this, first, it should be reminded that the probability of a soft gluon emission does not depend directly on the jet energy. Indeed, one can see on Fig 7.12 that the behavior of the soft tracks in a jet is almost jet energy independent (apart from some normalization effects as the fractions of gluon and quark jets change from $\sim 60\%$ to $\sim 20\%$).

Second, one needs to recall that color interference can be effectively accounted for (or visualized) as an angular ordering of emissions: emissions should occur at

subsequently decreasing angles. So, even if all emissions occur at the minimum k_T (it is natural to assume that the minimum k_T is of the order of $Q_{cutoff} = \Lambda_{QCD}$), then all further and further emitted gluons would have to have larger and larger energies. Eventually, such emissions are terminated as the result of phase space limitations and energy conservation. The larger the jet energy is, the farther away those limits are. Thus, as the jet energy increases, the multiplicity grows mostly due to the partons with higher and higher momenta and flying out at smaller and smaller angles.

Herwig was found to describe data very well for the whole range of particle momenta, apart from an overall normalization.

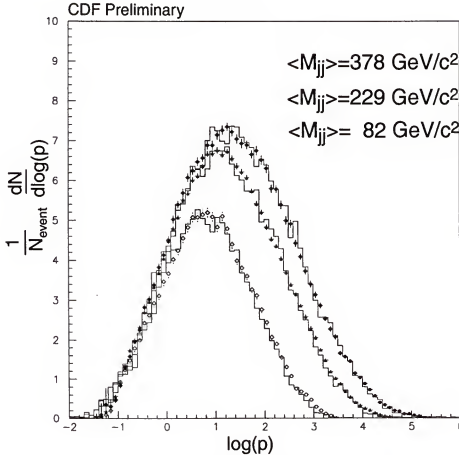


Figure 7.12: $dN/d\log p$ distribution for cone 0.47 and three dijet masses. Data is compared to the Herwig (plus QFL detector simulation) predictions. Herwig was scaled by 0.89.

7.4.4 Multiplicity Flow $dN/d\theta$

Figure 7.13 shows the differential $dN/d\theta$ distribution of tracks in a jet as obtained from the data, as well as the Herwig predictions (including the detector simulations). Clearly, the agreement between the two is nearly perfect.

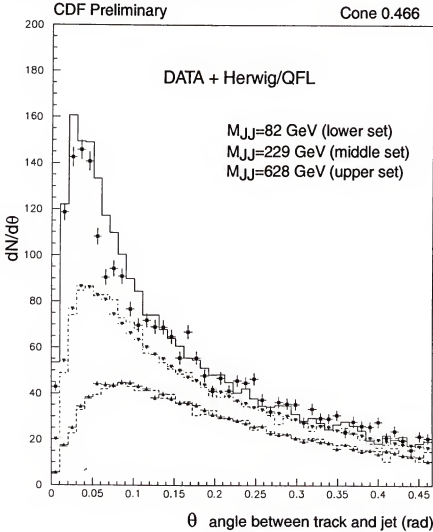


Figure 7.13: Multiplicity flow for three dijet masses and for the cone size 0.47. Data (points with error bars) is compared to Herwig Monte-Carlo plus detector simulation (histogram).

Herwig, as before, was scaled by 0.89. The same argument as in the case of the dN/dk_T distribution, leads to a conclusion that, without rescaling Herwig, the discrepancy between the data and the Monte-Carlo will be significant. Should one suspect that the corrections applied to data were not proper (e.g. the CTC losses are higher than expected), it would be hard to believe that these corrections were uniformly lower independently of the angle between the jet and the track. Track density is noticeably higher for smaller angles than for the large ones, and, therefore, losses there cannot be the same as in the large angle region.

7.5 Conclusions

Measurements performed in the course of this study show the dominant role of perturbative QCD in jet fragmentation. The agreement between the data and MLLA predictions holds for a wide range of jet energies.

The MLLA cutoff-scale Q_{eff} was measured from the shape of the momentum distributions (240 ± 40 MeV) and the peak position (256 ± 13 MeV) and agree with each other.

MLLA predicted $E_{jet} \sin \theta_c / Q_{eff}$ scaling is observed for the first time.

The LPHD parton-to-hadron conversion parameter K_{LPHD} is extracted from momentum distributions ($K_{LPHD}^{charged} = 0.58 \pm 0.09$) and, separately, from the inclusive mean charged particle multiplicity ($K_{LPHD}^{charged} = 0.57 \pm 0.11$). The two measurements are found to be in agreement with each other.

The ratio of multiplicities r is extracted using the shape of the distributions ($r=1.8\pm0.4$), as well as the total multiplicity ($r=1.7\pm0.3$), and found to agree.

The model independent measurement of r , not relying on the MLLA assumptions, resulted in $r=1.75\pm0.11\pm0.15$ and is in good agreement with the MLLA result, supporting the MLLA model of jet fragmentation.

Even though the qualitative agreement is good, there are quantitative discrepancies manifesting themselves in poor quality of the fits of the shape of the momentum distributions to MLLA. This indicates the presence of effects that are not described by MLLA+LPHD scheme.

Comparison of the data to Herwig Monte-Carlo has shown that Herwig overestimates the overall multiplicity of particles in jets by approximately 11%. Apart from this across the board scale problem, Herwig is shown to very well reproduce various properties of particles in jets.

CHAPTER 8

SUMMARY OF THE EXPERIMENTAL RESULTS AND THEIR IMPACT ON UNDERSTANDING OF JET FRAGMENTATION. FUTURE PERSPECTIVES

The results presented in this dissertation prove that perturbative QCD plays the dominant role in the jet fragmentation down to a very low scale $Q_{eff} \sim \Lambda_{QCD}$: the region that was long believed to be governed by the non-perturbative hadronization stage. Extensive tests of the predictions of the Modified Leading Log Approximation were performed and the theory was found to be in a very reasonable agreement with data.

Important model parameters were extracted using several methods. The MLLA cut-off scale Q_{eff} was measured using the inclusive momentum distributions of charged particles in jets for a range of dijet masses and several opening angles. The values obtained from the fits of the distributions ($Q_{eff}=240\pm40$ MeV) and from the evolution of the distribution peak position ($Q_{eff}=256\pm13$ MeV) are in agreement and have a plausible value: Q_{eff} , being the cut-off scale of the model, shows the low limit of the applicability of MLLA in terms of transverse momentum. Should this value be around 1 GeV, the conventional cut-off scale used in many perturbative QCD calculations, the vast majority of particles in jets would not be governed by the pQCD description forcing the fragmentation phenomenon to be outside the perturbative domain.

As it was mentioned before, the LPHD is believed to be correct in the asymptotic limit. The results of this study support the applicability of the Local Parton-Hadron Duality hypothesis already at currently achievable jet energies. The obtained value of the

parameter $K_{LPHD}^{charged}$ is in agreement with the desired approximately one-to-one rate of the parton-to-hadron conversion K_{LPHD} . From isotopic invariance, one would expect $K_{LPHD}^{charged}$ to be around and somewhat smaller than $2/3^1$. Measured value $K_{LPHD}^{charged}$ (0.57 ± 0.11 from the multiplicities, and 0.58 ± 0.09 from the fit of the momentum distributions) is in agreement with this expectation. $K_{LPHD}^{charged}$ can also be compared to a model-independent experimentally measured value: the fraction of energy carried by charged particles in jets with respect to the full jet energy. TASSO reported this ratio to be $f_{ch} = 0.61 \pm 0.02$ [38] in a good agreement with the measurement obtained in this study.

Regarding the ratio of multiplicities in gluon and quark jets r , the model dependent measurement obtained in this study ($r = 1.7 \pm 0.3$) is in agreement with the model-independent measurement of the same value $r = 1.75 \pm 0.11 \pm 0.15$. This agreement shows the self-consistency of the MLLA calculations and its consistency with the experimental data.

The data was compared to the predictions of Herwig Monte-Carlo. Herwig was found to be very successful in describing the properties of the particles inside jets. However, an overall rescaling of the particle multiplicity by 0.89 is preferred.

The evident success of the Modified Leading Log Approximation in describing the jet fragmentation greatly reduces the “gray” area in understanding the process of jet

¹ If all hadrons were pions, one would expect the charged particles to be $2/3$ of all. Presence of isodoublets, such as kaons, shifts this ratio towards $1/2$.

formation. Further opportunities to expand the range of the achievable jet energies will open with the upcoming run of the Tevatron at a new record center-of-mass energy of 2 TeV and a significant increase in the luminosity. This would allow expanding jet fragmentation studies by analyzing data with dijet mass energies above 600 GeV, the current limit. Data with higher jet energies will also allow obtaining samples of quark and gluon jets with higher level of purity than those currently achievable.

Another important study to be performed in the coming run is an accurate model-independent measurement of r , the ratio of multiplicities in gluon and quark jets, based on samples like photon (also Z - or W -boson) + one jet. High luminosity will allow collecting significant statistics for accurate measurement of r , verification of the predicted weak dependence of r on the jet energy, as well as comparison of various particle properties in quark and gluon jets (momentum distributions, jet shape etc.). These studies will significantly improve our understanding of the differences between gluon and quark jets.

Other studies that could be performed and that were left out of the scope of this study are related to the MLLA predicted momentum correlations for particles in jets and multiplicity fluctuations (KNO-scaling etc.). These measurements, being not simple inclusive distributions, would certainly make an important measurement improving our understanding of the extent of applicability of perturbative calculations to jet fragmentation.

And, finally, the improved MLLA calculations and, particularly, narrowing down the differences between the existing calculations (e.g. the 15-20% variation in the value of the parameter F_{nMLLA} as calculated by different working groups of theorists) will

allow better separation between the perturbative and the non-perturbative contributions into jet fragmentation.

APPENDIX

ANALYSIS OF THE CENTRAL TRACKING CHAMBER (CTC) RECONSTRUCTION EFFICIENCIES

One of the most serious difficulties of this analysis was associated with not well-known track reconstruction efficiency of the CDF Central Tracking Chamber. From very simple consideration, it is clear that the tracking algorithm should become less effective when track occupancies become large. Higher occupancy means that tracks are getting close to each other, hits produced by these tracks in the chamber can overlap and lead to incorrectly reconstructed or completely lost tracks.

Existing CTC efficiency parametrizations [40] were derived for very specific cases, such as with respect to soft leptons for the tagging of b-jets. Those parametrizations were obtained for particles in events with relatively low average track occupancies and are not appropriate for particles in jets. Straightforward crosschecks show that use of standard CDF efficiency parametrizations would result in unphysical trends in behavior, as a function of the jet energy, of the mean particle multiplicity and of the fraction of jet energy carried by charged particles.

Another reason suggesting necessity of a special study of the CTC tracking is the inappropriate, for our case, conventional definition of a “found” track. Traditionally, these kinds of studies are based on embedding additional hits, corresponding to a track with known parameters, into the raw CTC data banks, and then running full tracking reconstruction. If the track with expected parameters is reconstructed, this track is considered found. What to do if a track was reconstructed but with different parameters

than the embedded one? In many cases, when one searches for particles with particular properties, it is justifiable to consider such a track as a loss, simply because if this were a real particle, it would not pass the definition of the kind of particle one is looking for. The same reasoning will not work in case of particles in jets: if a particle was reconstructed with incorrect parameters, it would still be included into the analysis. This means that another definition of a “found” particle will be needed.

Complete parametrization of the CTC tracking efficiency for particles in jets may depend on many parameters, such as jet energy, how close a particular particle track is to the center of the jet, track momentum, how many other tracks are in the vicinity etc. Given that such detailed studies require large statistics and very substantial CPU time, an easier solution was found: not to derive a general parametrization but to find a correction function suitable for this particular data sample and not necessarily for arbitrary jet data.

From each of the 9 dijet mass bins of the original set of dijet data, a smaller subset was randomly chosen and used to find the required correction for this particular bin. All major parameters of the smaller samples were checked to be in reasonable agreement with corresponding full samples to ensure that selected sub-samples are statistically representative and do not introduce additional biases.

Track Embedding Method and Monte-Carlo Testing

The method adopted in CDF [40] of embedding tracks on a hit level into the DST format data (being next level after the raw data, this format preserves most of the low level information) with further full event re-tracking was used with standard production executable from OFFLINE reconstruction package (version 7.12). After that “old” tracks

(the ones that existed before embedding plus the track to be embedded) and “new” tracks (those found after retracking) can be compared to determine whether the track was found or not. As it was discussed above, the definition of success and failure may vary depending on what exactly is being studied. For the embedding procedure the C\$TRK routine CTADDH.CDF that embeds tracks with given helicity parameters into the CTC data bank was used. When re-running the tracking reconstruction, the VTPC and SVX data was not used (no track cross-detector matching was required). VTPC data was retrieved before re-tracking to determine parameters of the vertices, and then dropped. Exactly the same procedure was used when processing real data to avoid biases.

For track embedding, the CTC wire hit efficiency was adjusted layer-by-layer to have a reasonable agreement with real data. In [41], the hit efficiencies were adjusted on a wire-by-wire basis. In this analysis, the wires were adjusted collectively to reproduce the average superlayer hit efficiencies.

The goal of this study was not to get a general parameterization of CTC efficiency as a function of a large number of parameters, but to determine one particular correction function that will account for the CTC inefficiency effects and correct a particular distribution of interest (inclusive charged particles momentum spectrum, in our case). It was verified that tracks embedded into the events were not random but closely represent the pool of the real data tracks. The following algorithm was developed:

1. A real track from one of the jets in the event is picked;
2. The track is “reflected” into the second jet around the vertex point taking into account possible boost of the center-of-mass frame, and

adequately recalculating new track position with respect to the vertex (impact-parameter d , and dz);

3. Embed the “reflected” track with calculated parameters into the second jet;
4. Determine whether the track was found after re-tracking (unlike the usual determination of a found track we do not require the track to have parameters very close to the parameters of the embedded track). Remember parameters of both embedded and the matching newfound track;
5. Repeat the procedure with all tracks in the event (to avoid possible biases if track numbering in CTCs bank is not random);
6. Build a histogram containing parameters of all tracks that were embedded and found, possibly with different parameters, build another histogram containing parameters of the embedded tracks. Ratio of the two histograms gives desired correction function.

To verify the correctness of this approach, it was tested on a “toy” Monte-Carlo model. First, a number of events were generated with tracks distributed according to a particular function (sufficiently similar to the shape of the momentum distribution of particles in jets), and called the “true” distribution. Then, a special routine was used to lose tracks according to particular rules to obtain the “observed” distribution. The “true” and “observed” distributions were playing the roles of the real momentum spectrum of charged particles and the one affected by imperfectness of the CTC.

Then, the embedding algorithm was applied: tracks from the “observed” pool were embedded one-by-one into the opposite jet in the event. The same routine was losing the tracks producing “the 2nd order affected distribution”. Two histograms with parameters of the embedded and reconstructed tracks were built, and their ratio gave the desired correction function. This correction function was compared to the “true” correction function (the ratio of the “observed” and “true” distributions). The results are presented on Figure A.1.

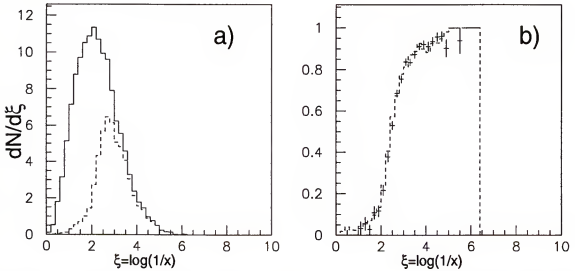


Figure A.1: Test of the algorithm based on a “toy” Monte-Carlo. Left plot shows the hypothetical initial track distribution (solid line) and the one affected by the “inefficiency”(dashed line). Right plot shows reconstructed efficiency (points with error bars) and the “true” efficiency (dashed line). Inefficiency was due to a combination of a smooth external function (all kinds of imperfections of the CTC) and a correlated loss of one or two tracks (with particular probabilities) if they are spatially close to each other.

Simulated track losses were coming from a combination of correlated and uncorrelated effects. For uncorrelated losses, a smooth function of the track angular direction was used (simulating inhomogeneous efficiency in different sectors of CTC). To study correlated effects, the distance between the given track and the one closest to it

was determined. Depending on how close these two tracks were to each other, one or both tracks could be lost with particular probabilities.

There are limits of applicability of this algorithm: reconstruction efficiency itself should not be very small (i.e. if all tracks of a particular sort were lost, the algorithm will not be able to say anything about them). Also, the tracks inside the bins should not have very different properties.

The second condition is satisfied for inclusive momentum distribution because of strong correlation between momentum and the position of the track with respect to the jet core. Nevertheless, for cross comparison, an “effective” efficiency correction was derived from the 2-dimensional correction, which involved as parameters not only ξ , but also the angle between the track and the jet axis. The two were found to agree.

Track-Finding Algorithm

As it was already mentioned above, the used here definition of a “found” track differs from the conventional one. The “found” track is not required to have the same parameters as the embedded one. This difference comes from the fact that we are not studying “what is the efficiency of finding particular track with correct parameters” but rather “how often we lose the track at all and how the tracks tend to change their parameters”.

Track finding was separated into two stages. At the first stage, a “human-like” algorithm was used. It was looking at the “old” (pre-existing tracks in the event plus the embedded track) and “new” tracks (those found after full re-tracking) and eliminating all pairs of tracks that were obviously the “old” and “new” version of the same track:

1. All “old” and “new” tracks within restricted cone 0.5 (a priori large angle) around the direction of the embedded track were identified and recorded;
2. One-by-one, all “old” tracks were checked for the presence of a close single “new” track, which could not be easily associated with any other “old” track¹. If such unambiguous matched pairs were found, they were eliminated from further consideration. The algorithm then proceeds to the next “old track repeating the search for a match and so on. At some point, the embedded track may be matched to its partner among “new” tracks. If this happens, the embedded track is considered “found”;
3. If all tracks in the vicinity of the embedded track are matched, and the embedded track has no partner, such a track is considered “lost”;
4. If neither of the cases described above took place, the algorithm proceeds to the next stage with a substantially simplified pattern of “old” and “new” tracks in the event;
5. Steps 1-3 are repeated several times with consecutively increasing size of the “close” definition. It does not help to repeat these steps many times because the saturation comes quite fast.

¹ Technically, to match and eliminate a pair of tracks we require them to have $|1/p_{old} - 1/p_{new}| < 0.004$, and the angle between the tracks $|\Delta\theta_{old-new}| < 0.002$. If there are no other “old” or “new” tracks within 3 times larger area, we eliminate both tracks from further consideration. If both particles have energy below 30 GeV, their charges are required to be the same. These cut-off parameters were obtained from the study of how far a pre-existing track can drift from its initial position as a result of re-tracking.

Figure A.2 (open circles are the “old” tracks, the embedded one is marked by a cross, dots represent tracks reconstructed after re-tracking) illustrates the algorithm described above by showing the typical track configurations one has to properly handle.

It is important to simplify the pattern recognition by eliminating obviously matching old and new tracks, and the first stage of the algorithm is designed to do exactly that, even though in a somewhat crude manner.

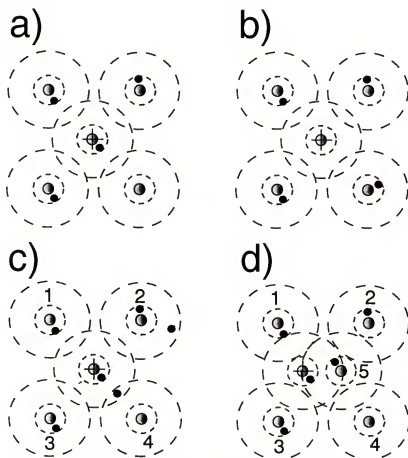


Figure A.2: Examples of the algorithm decision-making (stage I). “Old” tracks are denoted as the large gray circles, “new” tracks – as the black smaller circles, the embedded track is shown as an “old” track with a cross. a) The embedded track is found. b) The embedded track is lost. c) “Old” tracks 1 and 3 are eliminated with their “new” track partners, no decision made on the embedded one at this stage. d) “Old” tracks 1, 2, and 3 are eliminated with partner “new” tracks, no decision on the embedded one at this stage.

Before going further, the χ^2 was calculated² for all possible permutations of pairs of tracks. If $\chi^2 < 100$ (Figure A.4 justifies this cut-off) for any pair of “old” and “new” tracks, such pair is considered matched and eliminated (Figure A.3 a). Again, this step may eliminate the embedded track. In this case we consider it to be “found”.

In the second stage one usually had to deal with a fairly small number of tracks, and have a limited number of possible situations. The possible situations and corresponding actions were:

1. There were a few “new” tracks, an embedded track and no other “old” ones. The closest track (based on the χ^2) was chosen as a match, and the embedded track was considered “likely found”, and the χ^2 was recorded (Figure A.3 b);
2. A few “old” tracks, including the embedded one, and a “new” one. If the embedded track is the closest to the “new” one, it was considered “likely found” and the χ^2 was recorded. If the “new” one was close to another “old” track, the embedded track was considered “unlikely found” and the χ^2 was recorded with a negative sign. (Figs. A.3 c and A.3 d, where one needs to ignore the rightmost “new” track);
3. There were a few tracks of both kinds. A “new” track closest to the embedded one was identified, and it was checked if the opposite was true, i.e. whether the embedded one was the closest “old” track to the

² We used conventional definition of χ^2 : $\chi^2 = (\alpha_{new}^i - \alpha_{old}^i) (Cov^{-1})_{ij} (\alpha_{new}^j - \alpha_{old}^j)$, where α_{new} and α_{old} are the 5-vector helix of the “old” and “new” tracks, $\alpha = (\cos\theta, c, z0, d0, \phi0)$, and Cov is the covariance matrix of the “new” track.

chosen “new” one. If true, the track was assigned as “likely found” and the χ^2 was recorded. If not, the track was marked as “unlikely found” and the χ^2 was recorded with a minus sign. (Figs. A.3 c and A.3 d).

The vast majority of questionable events fell into a simple category 2. Others were distributed between the two others. Figure A.3 illustrates this part of the algorithm.

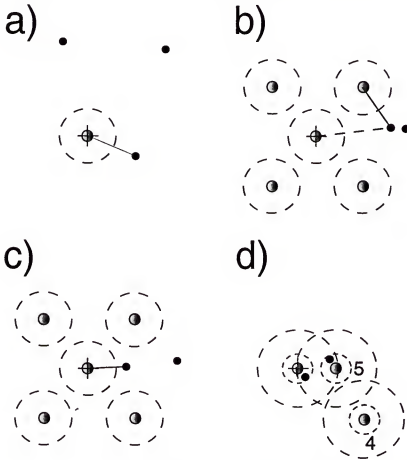


Figure A.3: Examples showing the second stage of the algorithm logic. a) The embedded track is “likely found”, χ^2 is recorded with a positive sign. b) “unlikely found”, χ^2 is recorded with a negative sign. c) “likely found”, χ^2 is recorded with a positive sign. d) If the χ^2 for the embedded one and the closest “new” track is less than 100 – “found”; if the χ^2 is greater than a 100 – “likely found”. recorded with a positive sign.

Figure A.4 shows the same distribution for those “likely” and “unlikely found” tracks. Three (out of nine available) different dijet mass samples are shown for each of the two cases.

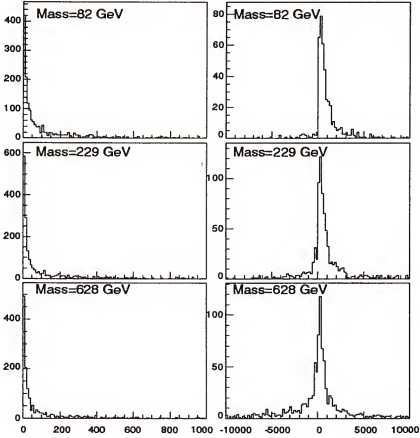


Figure A.4: χ^2 distribution for “unconditionally found” tracks (left) and for all others. Three dijet mass samples.

Results and Cross-Checks

Because of a relatively small size of the sample (about 400 - 450 events for each dijet mass sample), statistical errors were not negligible. If the bins in $\xi = \log(1/x)$ were

selected to be wide enough, the effects of tracks moving between bins (when parameters of the newfound track are far from the parameters of the embedded one) were small, and we dealt with a trivial binomial distribution.

To determine systematical errors in the efficiency determination, different ranges of χ^2 , suggested by Figure A.4 were considered, as shown in Table A.1. The “underestimated” efficiency was defined as when only unambiguously matched tracks (“found” column in Table A.1) were considered found. Conservatively one can interpret the tracks from the “likely found” category as the ones that were not lost but happened to have very different parameters.

Table A.1: Distribution of tracks among the categories.

Dijet Mass (GeV)	χ^2					
	Unlikely found		(Found)	Likely found		(Lost)
	$-\infty : -1000$	$-1000 : 0$		$100 : 1000$	$1000 : +\infty$	
81	0.34	0.13	88.73	2.72	2.10	5.98
105	0.35	0.37	87.50	2.65	2.51	6.61
140	0.53	0.22	89.47	2.30	1.91	5.57
182	0.92	0.53	87.45	2.57	2.65	5.87
228	1.13	0.68	85.24	2.97	3.11	6.86
292	1.87	0.74	84.33	2.52	3.17	7.37
378	2.67	1.09	80.66	2.79	4.02	8.77
487	3.73	1.48	79.07	2.46	4.64	8.61
628	4.84	1.54	75.88	2.64	5.16	9.94

The “best” efficiency was chosen to be determined by unambiguously matched tracks and also by those having $0 < \chi^2 < +1000$ (Figure A.4 justifies this choice). The “overestimated” efficiency was defined as the case when all matched tracks and those having $-1000 < \chi^2 < +\infty$ were considered found.

Figure A.5 shows the efficiency correction function for all nine dijet mass samples for tracks within cone 0.47 around the jet axis. Figure A.6 shows the efficiency correction for the tracks within cone 0.17. The shaded area represents the range of systematic error in the efficiency determination as defined above.

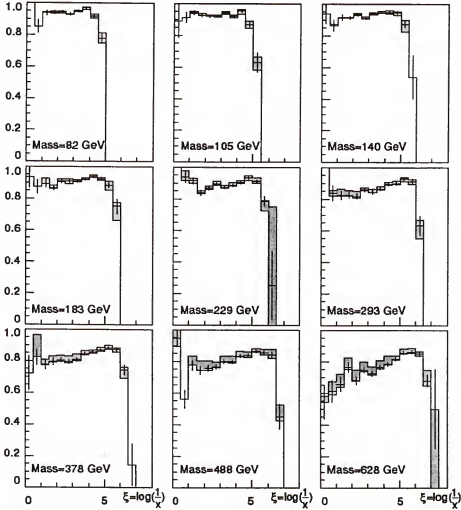


Figure A.5: CTC efficiency correction function (points with error bars) along with upper and lower limits that define the systematic error. Efficiency correction functions are calculated for tracks within cone 0.47 around the jet axis. Dijet mass ranges are shown.

The obtained efficiency was compared with the correction based on Q -factor parameterized efficiency [40], Figure A.7. It is obvious that the discrepancy becomes substantial for tracks in jets of energy above 150 GeV, but both agree for lower jet energies.

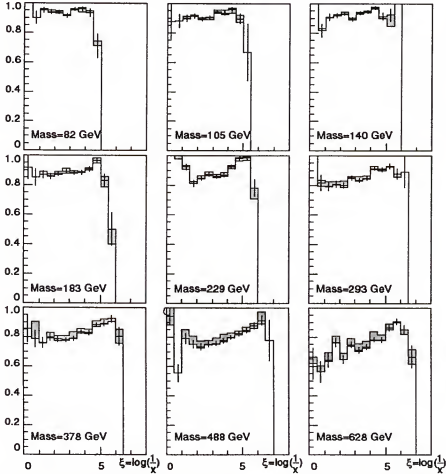


Figure A.6: CTC efficiency correction function (points with error bars) along with upper and lower limits that define the systematic error. Efficiency correction functions are calculated for tracks within cone 0.17 around the jet axis. Dijet mass ranges are shown.

For further cross-comparison of the results, the energy dependence of the ratio of energy carried by charged tracks was considered, within a particular angle around the jet axis, to the energy deposited in calorimeter (jet cone 0.7). First quantity was measured

entirely using CTC. The second one used calorimeter information. To determine the energy the standard module JTC96S [33] was used. Figure A.8 shows the results (error bars represent the statistical errors, shaded areas - range of the systematic uncertainty) along with the expectations based on Herwig + QFL detector simulation module (inverse triangle and a line). Results obtained using the efficiency based on [40] are also shown.

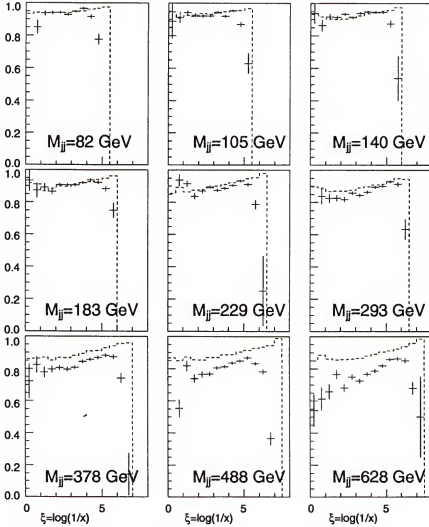


Figure A.7: CTC efficiency correction function (points with error bars) compared to efficiency correction obtained according to [40] (dashed-line histogram). Efficiency correction functions were calculated for tracks within cone 0.467 around the jet axis. Dijet mass ranges are shown.

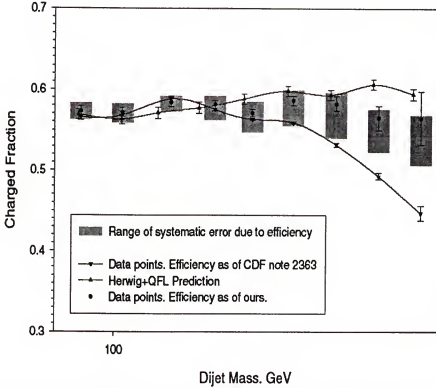


Figure A.8: Ratio of energy carried by charged tracks within restricted cone 0.47 around the jet direction to total jet energy deposited in calorimeter (jet defined with cone 0.7). Results obtained using the new efficiency correction (range of systematic uncertainty shown by shaded areas) and the efficiency in accordance with [40]. Both are compared to the Monte-Carlo predictions.

Conclusion And Limits of Applicability

The results obtained expand previous studies of CTC efficiency to include high-energy jet events. There is a systematic agreement between the new parametrization and results obtained earlier [40] at jet energies below 150 GeV (see Figure A.7). At larger energies, track losses become visibly larger than predicted by the previous studies [40], thus making this efficiency parametrization not usable.

There are indications that tracks at smaller cones are not completely recovered even with the proposed method. These tracks correspond to tracks in a very close vicinity of the jet core, where losses may be larger making the proposed approach less efficient.

However, the MLLA analysis to be carried out based on this efficiency deals with mostly soft hadrons and thus should not be significantly affected by the small remaining discrepancy.

LIST OF REFERENCES

- [1] S. Weinberg, Phys. Rev. Lett. 19, 1264 (1967); A. Salam, p. 367 of *Elementary Particle Theory* (ed. N. Svartholm), Almquist and Wiksells, Stockholm (1969); S. L. Glashow, J. Iliopoulos, and L. Maiani, Phys. Rev. D 2, 1285 (1970).
- [2] J.J. Lloyd, J. Fainberg and M. Schein, Phys. Rev. 80, 970 (1950).
- [3] J.L. Friedman and H.I. Kendall, Ann. Rev. Nucl. Part. Science 22, 203 (1972); M. Breidenbach et al, Phys. Rev. Lett. 23, 935 (1969).
- [4] J.D. Bjorken, Phys. Rev. 179, 1547 (1969).
- [5] R.P. Feynmann, *Photon-Hadron Interactions*, W.A. Benjamin, New York (1972).
- [6] M. Gell-Mann, Phys. Lett. 8, 218 (1964); G. Zweig, CERN-8419-TH-412 (1964).
- [7] M. Gell-Mann, Acta Phys. Austriaca Suppl. 9, 733 (1972); M. Han and Y. Nambu, Phys. Rev. B 139, 1006 (1965).
- [8] D.J. Gross and F. Wilczek, Phys. Rev. Lett. 30, 1343 (1973); H.D. Pollitzer, Phys. Rev. Lett. 30, 1346 (1973).
- [9] W. Bardeen, A.J. Buras, D.W. Duke and T. Muta, Phys. Rev. D 18, 3998 (1978).
- [10] CCFR Collaboration: W.G. Seligman et al., Phys. Rev. Lett. 79, 1213 (1997); NMC Collaboration: M. Arneodo et al., Phys. Lett. B309, 222 (1993); L.W. Whitlow, Ph.D. thesis, SLAC Report 357 (1990).

- [11] D.J. Fox et al., Phys. Rev. Lett. 33, 494 (1979).
- [12] V.N. Gribov and L.N. Lipatov, Sov. J. Nucl. Phys. 15, 438 (1972); L.N. Lipatov, Sov. J. Nucl. Phys. 20, 94 (1975); G. Altarelli and P. Parisi, Nucl. Phys. B 126, 298 (1977); Yu. L. Dokshitzer, Sov. Phys. JETP, 46, 641 (1977).
- [13] Yu.L. Dokshitzer, V.A. Khoze, A.H. Mueller, and S.I. Troyan. Rev. Mod. Phys. 60, 373 (1988).
- [14] V.S. Fadin, Sov. Journ. Nucl. Phys. 37, 245 (1983).
- [15] Yu. L. Dokshitzer and S. I. Troyan, Proc. 19th Winter School of the LNPI, Vol. 1, p. 144; Leningrad preprint LNPI-922 (1984); A.H. Mueller, Nucl. Phys. B 213, 85 (1983).
- [16] Ya. I. Azimov, Yu. L. Dokshitzer, V. A. Khoze and S.I. Troyan, Z. Phys. C27, 65 (1985); C31, 213 (1986).
- [17] V.A. Khoze and W. Ochs, Int. J. Mod. Phys. A 12, 2949 (1996).
- [18] D. Amati and G. Veneziano, Phys. Lett. B 83, 87 (1979); A. Bassetto, M. Ciafaloni and G. Marchesini. Phys. Lett. B 83, 207 (1979); G. Marchesini, L. Trentadue and G. Veneziano, Nucl. Phys. B 181, 335 (1981).
- [19] Yu.L. Dokshitzer, V.A. Khoze, A.H. Mueller, S. Troyan, *Basics of Perturbative QCD*, Editions Frontiers, France (1991).
- [20] S. Catani, Yu. L. Dokshitzer, F. Fiorani, B.R. Webber, Nucl. Phys. B 377, 445 (1992).
- [21] S. Lupia, W. Ochs, Nucl. Phys. (Proc. Suppl.) 64, 74 (1998).
- [22] I.M. Dremin, J.W. Gary, Phys. Lett. B459, 341 (1999).

- [23] JADE Collaboration: W. Bartel et al., Phys. Lett. B 123, 460 (1983); HRS Collaboration: M. Derrick et al., Phys. Lett. B 165, 449 (1985); MARK II Collaboration: A. Petersen et al., Phys. Rev. Lett. 55, 1954 (1985); TASSO Collaboration: W. Braunschweig et al., Z. Phys. C 45, 1 (1989); AMY Collaboration: Y.K. Kim et al., Phys. Rev. Lett. 63, 1772 (1989).
- [24] OPAL Collaboration: G. Alexander et al., Phys. Lett. B 265, 462 (1991); OPAL Collaboration: P.D. Acton et al., Z. Phys. C 58, 387 (1993); OPAL Collaboration: R. Akers et al., Z. Phys. C 68, 179 (1995); ALEPH Collaboration: D. Busculis et al., Phys. Lett. B 346, 389 (1995); OPAL Collaboration: G. Alexander et al., Phys. Lett. B 388, 659 (1996); ALEPH Collaboration: D. Busculis et al., Phys. Lett. B 384, 353 (1996); DELPHI Collaboration: P. Abreu et al., Z. Phys. C 70, 179 (1996); OPAL Collaboration: K. Ackerstaff et al., Eur. Phys. J. C 1, 479 (1998); DELPHI Collaboration: P. Abreu et al., Phys. Lett. B 449, 383 (1999); OPAL Collaboration: G. Abbiendi et al., Eur. Phys. J. C 11, 217 (1999); Y. Iwasaki, for SLD Collaboration, SLAC-PUB-6597, Aug 1994, Presented at DPF 94, Allbuquerque, NM; Y. Iwasaki, for SLD Collaboration, SLAC-R-95-460, SLAC Preprint, Stanford (1995).
- [25] CDF Collaboration: F. Abe et al., Phys. Rev. Lett. 65, 968 (1990).
- [26] CDF Collaboration: F. Abe et al., Phys. Rev. Lett. 70, 713 (1993).
- [27] CDF Collaboration: F. Abe et al., Phys. Rev. Lett. 74, 2626 (1995); D0 Collaboration: S. Abachi et al., Phys. Rev. Lett. 74, 2632 (1995).
- [28] *The Collider Detector at Fermilab, A compilation of articles reprinted from Nuclear Instruments and methods in Physics Research A*, North-Holland Physics publishing, Amsterdam, Holland (1988).
- [29] T. Sjostrand, Comp. Phys. Commun. 39, 347 (1986); T. Sjostrand and M. Bengtsson, Comp. Phys. Commun. 43, 367 (1987); T. Sjostrand, CERN preprint CERN-TH 6488/92.
- [30] T. Sjostrand, Comput. Phys. Commun. 82, 74 (1994).

- [31] G. Marchesini and B. R. Webber, Nucl. Phys. B 238, 1 (1984); 310, 461 (1984); G. Marchesini, B. R. Webber, G. Abbiendi, I. G. Knowles, M.H. Seymour and L. Stanco, Comp. Phys. Commun. 67, 465 (1992).
- [32] R.P. Feynmann and R.D. Field, Nucl. Phys. 136, 1 (1978).
- [33] M. Shapiro, A. Bhatti, J. Benlloch, R. Harris, T. Rodrigo, P. Sphicas, T. Westhusing, CDF Note 1810.
- [34] J. Huth, Proc. of the DPF 90 summer study on HEP, Snowmass, Colorado, World Scientific (1990).
- [35] CDF Collaboration: F. Abe et al., Phys. Rev D 45, 1448 (1992).
- [36] OPAL Collaboration: K. Ackerstaff et al., Z. Phys. C 75, 193 (1997); ALEPH Collaboration: D. Busculic et al., Z. Phys. C 73, 409 (1997); DELPHI Collaboration: P. Abreu et al., Z. Phys. C 73, 229 (1997); L3 Collaboration: M. Acciari et al., Phys. Lett. B 444, 569 (1998); TASSO Collaboration: W. Braunschweig et al., Z. Phys. C 47, 187 (1990); TPC Collaboration: H. Aihara et al., LBL-23727 (1988); MARK II Collaboration: A. Petersen et al., Phys. Rev. D 37, 1 (1988); AMY Collaboration: Y. Li et al., Phys. Rev. D 41, 2675 (1990).
- [37] H.L. Lai, J. Huston, S. Kuhlmann, F. Olness, J. Owens, D. Soper, W.K. Tung, H. Weerts, Phys. Rev D 55, 1280 (1997).
- [38] J. Huston, E. Kovacs, S. Kuhlmann, H.L. Lai, J.F. Owens, D. Soper, W.K. Tung, Phys. Rev. Lett. 77, 444 (1996).
- [39] J. F. Owens, FSU-HEP-910606 (1991).
- [40] JADE Collaboration: W. Bartel et al., Z. Phys. C 9, 315 (1981); CELLO Collaboration: H.J. Behrend et al., Phys. Lett. B 113, 427 (1982); TASSO Collaboration: M. Althoff et al., Z. Phys. C 22, 307 (1984); HRS Collaboration: D. Bender et al., Phys. Rev. D 31, 1 (1985).
- [41] OPAL Collaboration: G. Abiendi et al.: Eur. Phys. J. C 11, 217 (1999).

[42] A. Caner, A. Mukherjee and A. Yagil, CDF Note 2363.

[43] A. Warburton, CDF Note 4139.

BIOGRAPHICAL SKETCH

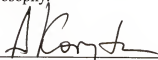
Alexei N. Safonov was born on April 23, 1973, in the city of Volzhsky in Russia. After graduating from high school in 1990, he continued his education in the Moscow Institute of Physics in Technology (State University).

In 1994 he received his Bachelor of Science degree (*summa cum laude*). In 1996 he received his master's degree *with highest distinction* from the same University. While studying in MIPT, he worked in the Theoretical Division of the Institute for the High Energy Physics with the Corresponding Member of Russian Academy of Sciences, Professor Semen S. Gershtein. Alexei's research work was related to the phenomenology of the electroweak interactions.

In the summer of 1996 Alexei N. Safonov became a graduate student in the Department of Physics, University of Florida. In 1997 he joined the CDF Collaboration and worked with Professors Andrey Korytov and Guenakh Mitselmakher on various aspects of experimental physics, particularly the jet fragmentation. In 1997-2001 Alexei took a critical part in design, construction, DAQ development, and commissioning of the Luminosity Monitor for the CDF Run II detector upgrade.

In 2001, Alexei N. Safonov graduated from the University of Florida with the degree of Doctor of Philosophy.

I certify that I have read this study and that in my opinion it conforms to acceptable standards of scholarly presentation and is fully adequate, in scope and quality, as a dissertation for the degree of Doctor of Philosophy.



Andrey Korytov, Chairman
Assistant Professor of Physics

I certify that I have read this study and that in my opinion it conforms to acceptable standards of scholarly presentation and is fully adequate, in scope and quality, as a dissertation for the degree of Doctor of Philosophy.



Guenakh Mitselmakher
Professor of Physics

I certify that I have read this study and that in my opinion it conforms to acceptable standards of scholarly presentation and is fully adequate, in scope and quality, as a dissertation for the degree of Doctor of Philosophy.



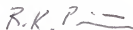
Richard Field
Professor of Physics

I certify that I have read this study and that in my opinion it conforms to acceptable standards of scholarly presentation and is fully adequate, in scope and quality, as a dissertation for the degree of Doctor of Philosophy.



John Yelton
Professor of Physics

I certify that I have read this study and that in my opinion it conforms to acceptable standards of scholarly presentation and is fully adequate, in scope and quality, as a dissertation for the degree of Doctor of Philosophy.



Robert Piña

Assistant Professor of Astronomy

This dissertation was submitted to the Graduate Faculty of the Department of Physics in the College of Liberal Arts and Sciences and to the Graduate School and was accepted as partial fulfillment of the requirements for the degree of Doctor of Philosophy.

May 2001

Dean, Graduate School